

INVESTIGATION OF INFLUENCING FACTORS IN LIQUID METAL
EMBRITTLMENT OF ADVANCED HIGH STRENGTH STEEL

by

DANIEL JOSEPH WOODSON MASSIE

LUKE N. BREWER, COMMITTEE CHAIR

MARK E. BARKEY

MARK L. WEAVER

A THESIS

Submitted in partial fulfillment of the requirements
for the degree of Master of Science
in the Department of Metallurgical and Materials Engineering
in the Graduate School of
The University of Alabama

TUSCALOOSA, ALABAMA

2019

Copyright Daniel Joseph Woodson Massie 2019
ALL RIGHTS RESERVED

ABSTRACT

This thesis explored the influence of temperature, steel type, galvanization method, and macro-strain level on the sensitivity of advanced high strength steels (AHSS) to zinc-based liquid metal embrittlement (LME). It is critical to understand the influencing factors of LME because zinc coatings are commonly used to protect steel parts from corrosion, and the use of advanced high strength steel in the automotive industry is increasing. Electro-galvanized and zinc free samples of a transformation induced plasticity steel, TBF1180, and a complex phase steel, CP1200, were studied to examine the sensitivity of each to LME. Hot-dip galvanized samples of CP1200 were examined alongside the electro-galvanized samples to investigate the effect of coating method on the LME effect. Hot tension tests were performed and ductility trough graphs were created for all samples to examine the effect of these factors on LME during fracture. Additionally, small-strain tensile tests were designed and performed on the steels to examine LME crack nucleation. From the results it was determined that LME response is temperature and steel dependent. It was shown that TBF 1180 nucleated LME cracks at 600 °C while CP1200 did not. It was also determined that hot-dip galvanized coatings more readily nucleate LME cracks than electro-galvanized coatings. Finally, these results suggest that macro-plastic deformation may not be required to initiate an LME response.

LIST OF ABBREVIATIONS AND SYMBOLS

°C	Degrees Celsius
μm	Micrometer
AHSS	Advanced high strength steel
Al	Aluminum
A1	Equilibrium eutectoid temperature
A3	Equilibrium ferrite to austenite phase transformation
B	Boron
Bi	Bismuth
Bs	Bainite start temperature
C	Carbon
CP	Complex phase
Cr	Chromium
Cu	Copper
DP	Dual phase
EDS	Energy dispersive x-ray spectrometry
EG	Electro-galvanized
Fe	Iron
g/L	Grams per liter
Ga	Gallium
GI	Pure-Zinc hot-dip galvanized

GPa	Giga Pascal
keV	Kiloelectron volt
KGA	Krishtal-Gordon-An
LME	Liquid metal embrittlement
Ms	Martensite start temperature
Mg	Magnesium
Mn	Manganese
Mo	Molybdenum
MPa	Mega Pascal
mm	Millimeter
N	Nitrogen
Ni	Nickel
Nb	Niobium
P	Phosphorus
Q&P	Quench and partition
S	Sulfur
SE	Secondary electron
Si	Silicon
SJWK	Stoloff-Johnson-Westwood-Kamdar
TBF	Transformation induced plasticity bainitic-ferritic
TEM	Transmission electron microscopy
Ti	Titanium
TRIP	Transformation induced plasticity

TWIP

Twinning induced plasticity

V

Vanadium

wt. %

Weight percent

Zn

Zinc

ACKNOWLEDGMENTS

The author gratefully acknowledges the counsel, critiques, and guidance from his advisor, Dr. Luke N. Brewer. The author would like to thank Ning Zhu for his assistance and support in this work, and specifically in SEM imaging. The author would also like to thank Mitchell Roze for his support in this work, specifically in sample preparation. The author acknowledges Nathaniel Briant for sharing his knowledge of Gleeble operation.

This research is financially supported by Daimler-Benz and MBUSI. We are very grateful for the support and collaboration of H. Schubert and B. Hilpert at TecFabrik and J. Cousineau at MBUSI.

CONTENTS

ABSTRACT.....	ii
LIST OF ABBREVIATIONS AND SYMBOLS.....	iii
ACKNOWLEDGMENTS.....	vi
LIST OF TABLES.....	viii
LIST OF FIGURES.....	ix
BACKGROUND AND MOTIVATION.....	1
THESIS OBJECTIVES.....	13
EXPERIMENTAL METHODS.....	15
RESULTS.....	21
DUCTILITY TROUGH TESTING.....	21
SMALL STRAIN TESTING.....	29
DISCUSSION.....	42
CONCLUSION.....	53
REFERENCES.....	55

LIST OF TABLES

Table I. Summary of AHSS generations and their properties in literature.....	7
Table II. Chemical compositions by weight percent of TBF1180 and CP1200.....	15
Table III. Experimental Young's moduli at high temperature for TBF1180 and CP1200 compared with literature on Grade 22 steel and S355J2H structural steel.....	32

LIST OF FIGURES

Figure 1. Thermal processing cycle for the creation of TBF steel.....	5
Figure 2. Thermal processing cycle for the creation of Q&P steel.....	6
Figure 3. Comparison of tensile strength and elongation at failure of AHSS and traditional steels.....	8
Figure 4. Large LME cracks formed at the weld shoulder during resistance spot welding of TBF1180.....	10
Figure 5. Geometry of the sample used for small strain testing of EG CP1200 and ductility trough testing of all steels.....	16
Figure 6. Geometry of the EG TBF1180 and GI CP1200 sample used for small strain testing...	16
Figure 7. Experimental setup for ductility trough Gleeble hot-tension testing.....	17
Figure 8. Experimental setup for small strain Gleeble hot-tension testing.....	18
Figure 9. Example thermomechanical cycle for 0.2mm displacement test at 800 °C.....	19
Figure 10. Temperature effect on ductility as measured by fracture strain for EG TBF1180.....	22
Figure 11. SE images of the fracture surface of EG TBF1180 at 600 °C showing brittle intergranular fracture on half of the sample (a) low magnification (b) high magnification.....	23
Figure 12. SE images of the fracture surface of EG TBF1180 at 800 °C showing brittle intergranular fracture through the sample (a) low magnification (b) high magnification.....	24
Figure 13. Temperature effect on ductility as measured by fracture strain for EG CP1200.....	25
Figure 14. Temperature effect on ductility as measured by fracture strain for GI CP1200.....	26
Figure 15. SE images of the fracture surface of GI CP1200 at 600 °C showing substantial necking (reduction in area) and micro-voids (a) low magnification (b) high magnification.....	27

Figure 16. SE images of the fracture surface of GI CP1200 at 800 °C showing necking and brittle fracture in different areas (a) low magnification (b) high magnification.....	28
Figure 17. Small strain testing of EG TBF1180 (top) 600 °C (bottom) 800 °C.....	30
Figure 18. Small strain testing of EG CP1200 (top) 600 °C (bottom) 800 °C.....	31
Figure 19. Small strain testing of GI CP1200 (top) 600 °C (bottom) 800 °C.....	32
Figure 20. Stress strain curve of GI CP1200 with Young's modulus at 0.2% strain offset.....	33
Figure 21. BSE images of the zinc-steel interface of 800 °C 0.3mm stroke test (a) EG TBF1180 0kN cooling (b) EG TBF1180 (c) GI CP1200 (d) EG CP1200.....	35
Figure 22. BSE images of the zinc-steel interface of 600 °C 0.3mm stroke test (a) EG TBF1180 (b) GI CP1200 (c) EG CP1200.....	36
Figure 23. BSE images of the zinc-steel interface of 800 °C 0.2mm stroke test (a) EG TBF1180 (b) GI CP1200 (c) EG CP1200.....	37
Figure 24. BSE images of the zinc-steel interface of 600 °C 0.2mm stroke test (a) EG TBF1180 (b) GI CP1200 (c) EG CP1200.....	38
Figure 25. BSE images of the zinc-steel interface of 800 °C 0.1mm stroke test (a) EG TBF1180 (b) GI CP1200 (c) EG CP1200 (black arrows point to small cracks at the surface).....	39
Figure 26. BSE images of the zinc-steel interface of 600 °C 0.1mm stroke test (a) EG TBF1180 (b) GI CP1200 (c) EG CP1200.....	40
Figure 27. (a) BSE image of 0.2mm 800 °C GI CP1200 sample with white box indicating area examined with EDS (b) EDS results for this area with red indicating zinc-rich areas.....	41
Figure 28. The simplified structure of hot-dip galvanized steel adapted from.....	46
Figure 29. The progression of the zinc-steel interface at increasing temperature.....	47
Figure 30. Stress versus strain of failure testing of GI CP1200 with different sample preparation methods at 800 °C.....	50
Figure 31. Temperature effect on ductility as measured by fracture strain for GI CP1200 for different sample preparation methods.....	50

Figure 32. Elastic region of room temperature test of TRIP700 steel with linear fit (red) and a 1kN preload.....52

BACKGROUND AND MOTIVATION

In recent years, advanced high strength steels (AHSS) have been a key area of research and investment for the automotive industry. AHSS are classified as having yield strengths greater than 300 MPa and tensile strengths greater than 600 MPa (De Cooman, 2004). It is expected that as the strength of a material increases its ductility will drop and vice versa (Chen, Zhao, & Qin, 2013). This is not always true however. Modern AHSS have shown the ability to produce high strength values while maintaining relatively high ductility and formability (Bachmaier, Hausmann, Krizan, & Pichler, 2013). There are three factors which have largely influenced the industrial focus on AHSS research: the desire for light-weighting, the necessity for increased vehicle safety, and the production concerns encountered with other materials (De Cooman, 2004). Light-weighting is the process by which an automobile's gross weight is reduced without compromising its structural integrity. This overall reduction in vehicle weight is desirable, as it has been proven to reduce both the greenhouse gas emissions and fuel consumption of a vehicle over its lifetime (Kim, Kim, Kim, Chung, & Choi, 2014). AHSS provide a simple solution to this problem, as their superior strength allows for less material to be used for the same application when compared to traditional automotive steels. Vehicle safety, especially in non-ideal crash situations where the crumple zones are not fully engaged, is heavily dependent on the area of the frame around the cabin of the vehicle. This area, known as the passenger safety cage, must be constructed of strong materials capable of maintaining rigidity during impact, and this requirement is well matched by AHSS (De Cooman, 2004).

AHSS face competition in these areas, however. Other light-weight materials, such as certain aluminum and magnesium alloys and high-strength composites can meet the light-weighting and vehicle safety requirements mentioned above. These materials are, however, limited by issues they face in production that AHSS do not. For one, aluminum and magnesium alloys do not meet the high strength and stiffness offered by AHSS. The maximum tensile strength for aluminum alloys is approximately 550 MPa and the Young's moduli range from 68 GPa to 82 GPa. The values for magnesium alloys are lower with a maximal tensile strength of 475 MPa and Young's moduli ranging from 42 GPa to 47 GPa (Cambridge, 2003). For both aluminum and magnesium alloys the highest listed tensile strength falls below the 600 MPa tensile strength that defines the minimum requirements for an AHSS (De Cooman, 2004). Additionally, Young's moduli greater than 204 GPa are seen in AHSS which more than doubles the highest Young's modulus seen in aluminum and magnesium alloys (Silva et. al., 2016). Because of this difference in mechanical properties, more material must be used when building with aluminum and magnesium alloys, and this bulk can alter vehicle designs and increase raw material cost. Additionally, these materials are more expensive to produce than high strength steels (Motavalli, 2012). Finally, these materials face joining and production issues not encountered by AHSS, making them less cost effective for production overall (De Cooman, 2004).

AHSS can be divided into three generations by composition, microstructure, and dominant strengthening mechanism. The first generation of AHSS's is comprised of complex phase (CP) steels, low-alloy transformation induced plasticity (TRIP) steels, and dual phase (DP) steels. This first generation meets the strength requirements to be classified as an AHSS but shows the lowest ductility of the three generations (Lee & Han, 2015). Compositionally, CP

steels typically have small amounts of Nb, Ti, or V. The microstructure of CP steels is defined as being primarily composed of fine ferrite or bainite with a high volume of martensite (Kuziak, Kawalla, & Waengler, 2008). The low-alloy TRIP steels have less than 3.5 wt.% alloying elements, the most important of these being manganese as it promotes austenite formation. Their microstructure is a composite structure of ferrite, bainite, and retained austenite (De Cooman, 2004). These TRIP steels are primarily strengthened by the TRIP effect, in which plastic deformation causes the retained austenite in the microstructure to transform into martensite. This transformation relieves concentrated stresses, delays necking, and increases the work hardening coefficient as austenite is replaced by significantly harder martensite (De Cooman, 2004). The final first generation AHSS, DP steel, is defined by a primary ferrite matrix with a secondary martensite phase. This structure allows for a high tensile strength but relatively low yield stress causing DP steels to be readily formable (Cai, Liu, & Liu, 2014). This first generation shows higher strengths than traditional steels, but a low average elongation at failure of approximately 20% led to the development of further generations of AHSS (Lee & Han, 2015).

The second generation of AHSS is defined by the production of high-manganese twinning induced plasticity (TWIP) steels. The high manganese content stabilizes a fully austenitic microstructure, allowing for plastic deformation by twinning (Bouaziz, Allain, Scott, Cugy, & Barbier, 2011). When twinning occurs the mean free path available to dislocations decreases. This creates an effect similar to that seen in the Hall-Petch effect where decreases in grain size limit dislocation motion and increase strain hardening and tensile strength (De Cooman, Estrin, & Kim, 2018). This effect leads to excellent mechanical properties with strengths over 700 MPa and elongation at failure exceeding 50% (Lee & Han, 2015). Despite these desirable mechanical properties, certain issues have made these steels less suitable for

production use. High-manganese TWIP steels have been found to be difficult to weld, preventing their implementation (Bouaziz, Allain, Scott, Cugy, & Barbier, 2011). Additionally, the high volume of manganese necessary for the production of these steels significantly increases the production cost of these steels (Lee & Han, 2015). Together these problems necessitated the development of the third generation of AHSS's.

The third generation of AHSS are designated by the complex thermal cycling the steels undergo during production. The effect of this cycling combines with the effects of alloying composition to produce unique microstructures. Two examples of this are TRIP assisted bainitic ferritic (TBF) and quench and partitioning (Q&P) steels. TBF steels have lower manganese content than first generation TRIP steels, but still enough to produce retained austenite and trigger the TRIP effect. (Lee & Han, 2015). The microstructure of a TBF steel consists of retained austenite in a hard, bainitic matrix. This harder, bainitic matrix leads to higher yield strengths than those seen in first generation TRIP steels (with a ferrite matrix). This microstructure is formed from the multi-stage heat treatment illustrated in Figure 1. The steel is first heated above its austenization temperature until fully austenized. It is then rapidly cooled below the bainite formation temperature, but importantly above the martensite formation temperature. It is held at this temperature for 1 to 5 minutes before being rapidly quenched to room temperature (Hausmann, 2014). During the second holding stage of this process the carbon is distributed throughout the steel. This is critical, as the carbon enrichment stabilizes the austenite and prevents it from transforming into austenite during the final quench (Zaefferer, Ohlert, & Bleck, 2004).

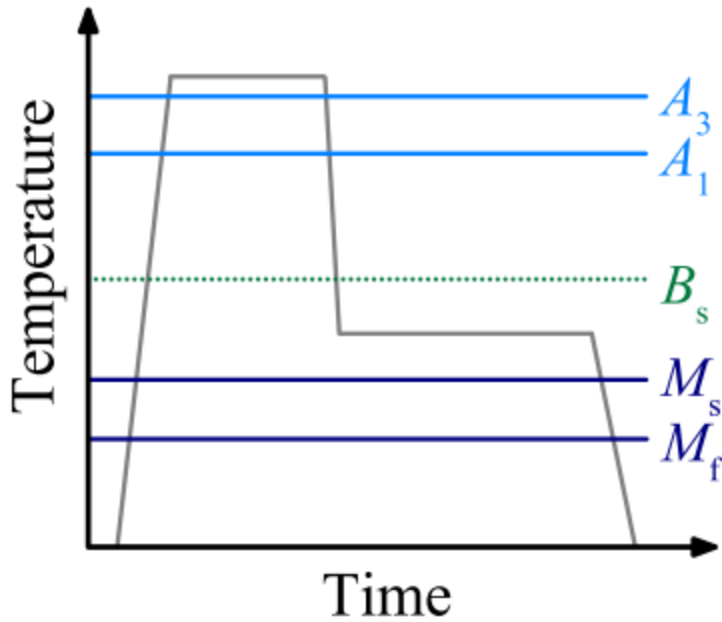


Figure 1. Thermal processing cycle for the creation of TBF steel (Hausmann, 2014).

Q&P steels are typically alloyed with carbon, silicon, and either manganese or aluminum and are subjected to the quench and partition heat treatment (Wang & Speer, 2013). This process involves quenching the steel below its martensite start temperature. This causes the carbon to partition from the martensite, which helps stabilize the remaining austenite. It is then aged at temperatures at or higher than the initial quench temperature. This results in a microstructure of ferrite and a stabilized austenite phase that contains martensite laths (Edmonds et al., 2006). In general, these third generation AHSS show the expected high strengths and moderate ductility when compared to the other generations of AHSS (Lee & Han, 2015). Figure 2 shows the Q&P thermal cycle, table I summarizes the three generations of AHSS, and Figure 3 shows a comparison of the mechanical properties of the three generations of AHSS as well as some traditional steels.

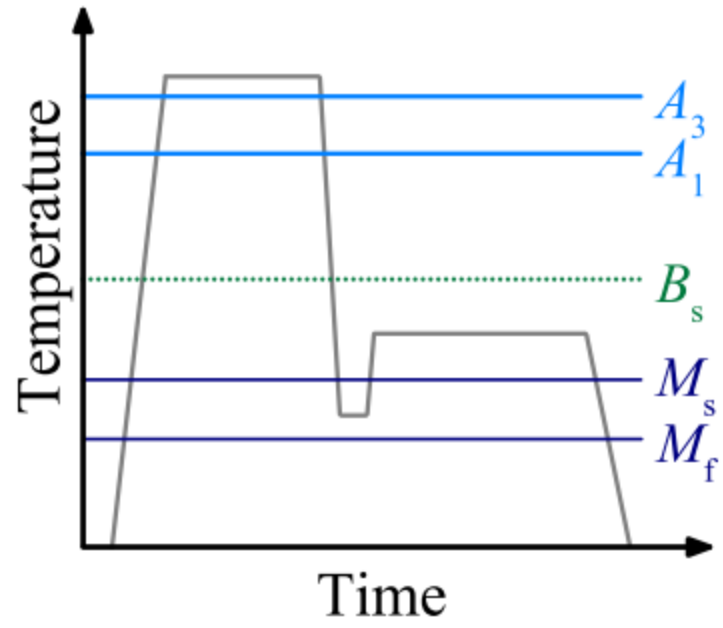


Figure 2. Thermal processing cycle for the creation of Q&P steel (Hausmann, 2014).

Table I: Summary of AHSS generations and their properties in literature

Generation I AHSS				
	Key Compositional Additions	Phases present	UTS Range (MPa)	% Elongation
DP Steels	Si, P, Mn, Cr	Primary Ferrite & Secondary Martensite	600-1000	<20%
CP Steels	Nb, Ti, V	Fine Ferrite or Bainite with High Volume of Martensite	600-1200	<20%
TRIP Steels	< 3.5% Total C, Si, Mn, Al	Ferrite, Bainite, Retained Austenite	700-900	<35%
Generation II AHSS				
TWIP Steels	$\geq 17\%$ Mn	Fully Austenitic	650-1200	50-70%
Generation III AHSS.				
TBF Steels	1.5-2.5% Mn	Retained Austenite in Bainite Matrix	1000-1400	10-30%
Q&P Steels	C, Si, & Mn or Al	Ferrite & Retained Austenite with Martensite Laths	800-1700	10-25%

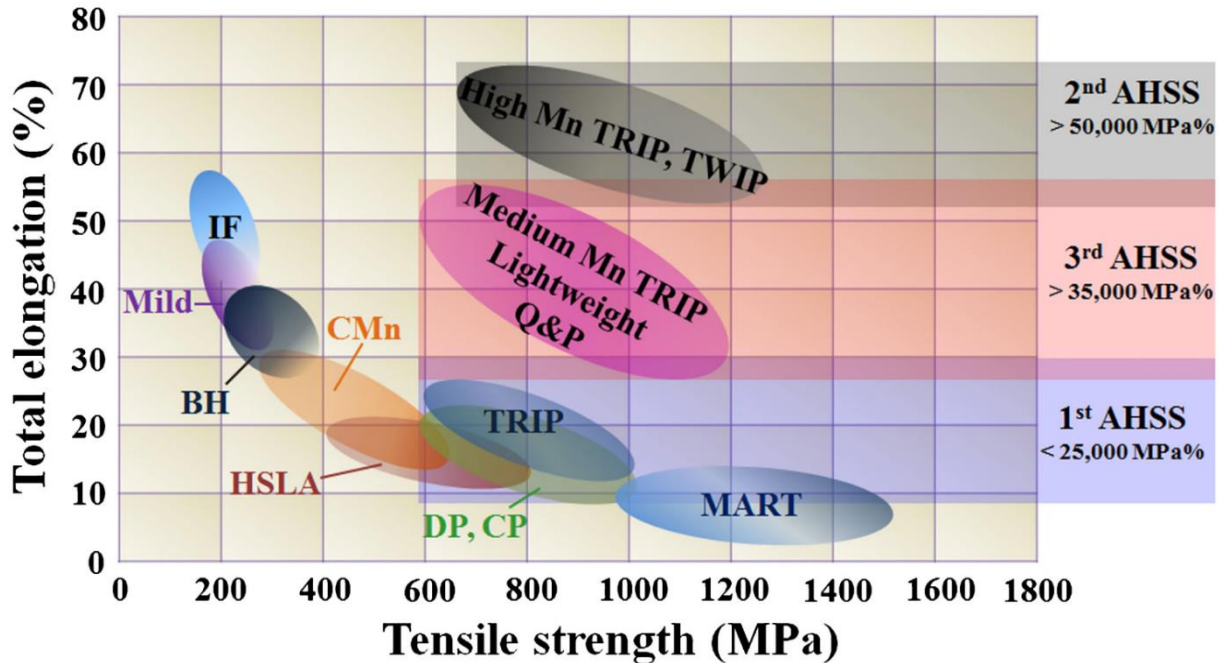


Figure 3. Comparison of tensile strength and elongation at failure of AHSS and traditional steels (Lee & Han, 2015).

As can be seen above, AHSS show significant improvements in strength and ductility when compared to traditional steel alloys and therefore show potential for use in the automotive industry. Where the complications arise, however, is in the additional processes necessary for automotive use, namely galvanization. This is primarily done in one of two ways, hot-dip galvanization and electro-galvanization. In hot-dip galvanization the steel is submerged in molten zinc in order to form a zinc coating on the steel surface, whereas in electro-galvanization the steel is submerged in a solution containing zinc sulfate electrolytes with a zinc anode and a current is run through the system causing zinc to plate the steel (American Galvanizers Association, 2011). This zinc coating acts as a sacrificial anode, helping to protect the steel from corrosion (Marder, 2000). These galvanization methods can lead to a complex intermetallic structure forming between the zinc and steel. This is especially true for the hot dip process where as many as four unique intermetallic layers have been seen (Mita, Ikeda, & Maeda, 2013). While

this zinc coating is necessary for corrosion protection, it has been shown to react unfavorably with certain steels during the manufacturing leading to a decrease of mechanical properties in a process known as liquid metal embrittlement (LME) (Bhattacharya, 2018).

The phenomenon of LME was discovered in the 1870s and has been documented in the interaction of a number of material pairings including Al-Ga, Ni-Bi, and Cu-Bi (Bhattacharya, 2018). It is agreed that for LME to occur both tensile stresses and the liquid metal of interest must be present (Joseph, Picat, Barbier, 1999). Importantly, LME has been found to occur with the pairing of liquid zinc and certain steels. The work by Beal et. al. showed LME to be abundant in fully austenitic TWIP steels (Beal, Kleber, Fabregue, & Bouzekri, 2012). Other work has shown this same LME sensitivity in certain TRIP, TBF, and CP steels (Briant, 2018).

Where LME becomes an issue in automotive manufacturing is during welding of galvanized steel sheets, as the process produces the liquid zinc and tensile stresses required for LME in the area around the weld nugget. Once the steel is weakened by LME, surface cracks can readily form, though this behavior has been seen to be steel dependent (Bhattacharya, 2018). Figure 4 shows a series of large LME cracks created in the heat affected zone during resistance spot welding of TBF1180 steel.

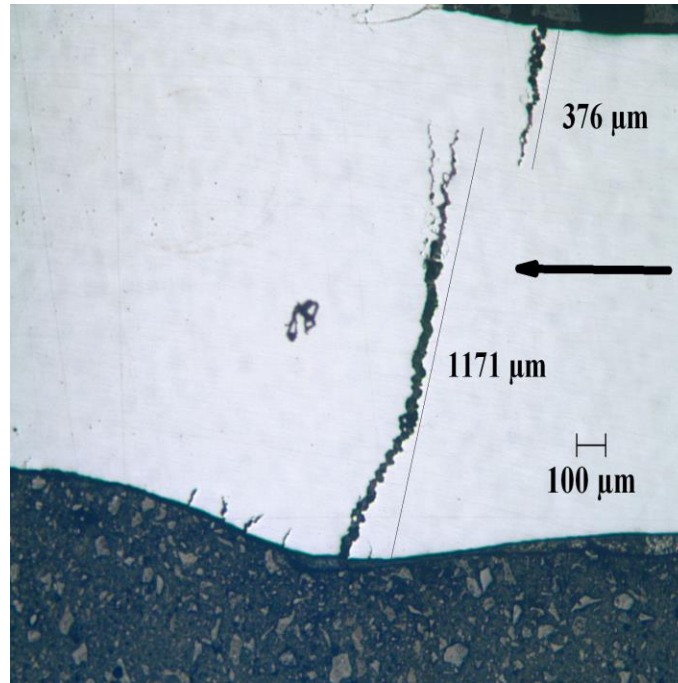


Figure 4. Large LME cracks formed at the weld shoulder during resistance spot welding of TBF1180

While LME has been shown to occur in a wide variety of steels and to varying degrees of intensity, the mechanism by which LME occurs is not fully understood. Three of the main groups of models proposed for the controlling mechanism in LME are dislocation activity models, crack tip brittle fracture propagation models, and grain boundary diffusion models. Kang et al. have provided an excellent review of these mechanisms in their 2016 paper on LME testing of galvanized steels. A shared trait of all of these cracking methods is that the liquid zinc is able to rapidly move to the crack tip as the crack grows, constantly supplying zinc (Kang H., Cho, Lee, & De Cooman, 2016). The dislocation activity models focus on the activity of dislocations at the crack tip in the presence of the embrittling liquid. The Lynch and Rebinder-Popovich models both suggest that the liquid metal enhances the emission of dislocations due to a lowering the stress required for dislocation production. Though the models share this assumption, they differ in their supposition of how the crack propagates. The Lynch model predicts that the

adsorption of liquid metal atoms at the crack tip will encourage the formation of dislocations causing localized slip. These dislocations will then be injected into the material just ahead of the crack tip or into the voids formed at particles in a plastic zone ahead of the crack causing the crack to propagate (Lynch, 1988). The Rehbinder-Popovich model shares the enhanced dislocation assumption of the Lynch model and suggests that this increase in dislocation emission will increase the dislocation density at the interface of the liquid and base metal, and this will result in local work hardening of the surface. This hardened area then forms microcracks which proceed rapidly through the work-hardened material, slowing when they reach the ductile base material (Popovich, 1979). The third proposed model for dislocation activity was brought forth by Hancock and Ives and suggests that plastic deformation ahead of the crack tip forms dislocation pileups at grain boundaries. These pileups are said to interact with atoms from the liquid metal diffusing forward of the crack tip causing embrittlement (Hancock & Ives, 1971). In all of these cases plastic deformation is necessary for LME to occur.

The second set of models can be collectively described as brittle fracture crack propagation models. In these models the liquid metal weakens the atomic bonding of base metal and the material is said to fail through brittle fracture. There are three models that fall into this category. The first, the Rostoker-Rehbinder model, suggests that the surface energy of the base metal is lowered by the adsorption of the liquid metal. This in turn reduces the fracture strength of the material. It is assumed that fracture is initiated by sub-surface slip generating dislocation pileups at the interface between the liquid and base metals. The crack then propagates by breaking the bonds of the atoms at the crack tip (Rostoker, McCaughey, & Markus, 1960). This model was expanded on in the Stolof-Johnson-Westwood-Kamdar (SJWK) model. The SJWK model suggests that the liquid metal weakens the bonding of the base metal through

chemisorption. These weakened bonds then break and the crack propagates, though it must be noted that this model does not predict plastically deformed fracture surfaces (Westwood & Kamdar, 1963). The third and final crack tip brittle fracture model was proposed by Robertson and Glickman and supposes that atoms from the base metal are dissolved into the liquid metal at the tip of the crack. As such, LME is treated as a form of stress corrosion cracking and is treated as a function of the solubility of the base metal in the liquid metal and is increased by factors such as surface roughness. This model does not seem to require plastic deformation to occur (Glickmann, 2011).

The third and final group of LME models assumes crack growth to be driven by grain boundary diffusion. This model differs from the previous set of models, as it does not require the crack tip to be wetted by liquid embrittling metal. The Krishtal-Gordon-An (KGA) model describes the penetration of embrittling atoms as a three-stage process. First, liquid metal atoms are adsorbed on the surface of the base metal. Next, these atoms undergo stress-assisted grain boundary diffusion until reaching a critical value, and, finally, the material fails as the crack resistance of the grain boundary lowers. The KGA model describes LME as a solid-state diffusion process, and further states that no plastic deformation is necessary at the crack tip (Gordon & An, 1982). The other grain boundary diffusion model was proposed by Klinger and Rabkin. In their model, high stresses generated by the Kirkendall effect during solid-state grain boundary diffusion lead to intergranular fracture. As these grain boundaries open up more liquid metal penetrates causing this effect to continue. This model also shows no need for plastic deformation (Klinger & Rabkin, 2011).

While there are many models for the LME of zinc-coated steels, none is universally accepted. Some work has shown faults in the dislocation activity model, as examinations of

fracture in TWIP steel showed no dislocation pileup at the fracture surface (Kang H., Cho, Lee, & De Cooman, 2016). This same work also showed a strong presence of LME in the area of formation of the Γ ($\text{Fe}_3\text{Zn}_{10}$) intermetallic in TWIP steels. Another study on the microcracking of galvanized high manganese TWIP steel found that the transformation of the zinc-iron boundary layer was vital to the formation of microcracks in the steel surface, as the cracks grew along the grain boundaries of zinc rich ferrite grains as they formed from the same Γ intermetallic (Kang J., Kim, Kim, & Kim, 2019).

This thesis examines the origin of LME cracks for galvanized CP and TBF steels. The literature clearly has not established whether plastic deformation is necessary for the formation of LME cracks. This thesis will perform hot tension experiments in both the macro-elastic and macro-plastic regimes to determine whether plastic deformation is a requirement for LME in these AHSS. In addition, the role of the type of galvanized coating will be examined for the same CP steel.

Thesis Objectives

- **Determine the range of temperatures over which CP and TBF steels experience the loss of ductility associated with liquid metal embrittlement.** Using the Gleeble thermomechanical tester, hot tension tests are performed over a range of temperatures on bare and galvanized samples of each steel. The fracture strains obtained from these tests are used to assess the LME behavior of these steels.
- **Determine whether macro-plastic deformation is necessary for liquid metal embrittlement cracks to form in advanced high strength steels.** Using the Gleeble thermomechanical tester, small total strain experiments from below 0.001 strain to above

0.014 strain can be performed at high temperature to determine what conditions are necessary for LME to initiate.

- **Determine whether the method of galvanization affects the liquid metal embrittlement behavior of an advanced high strength steel.** Both low strain, and fracture tests are performed on samples of hot-dipped and electro-galvanized CP1200 steel.

EXPERIMENTAL METHODS

The materials investigated in this thesis are electro-galvanized (EG) TBF1180, EG CP1200, and hot-dipped pure Zn galvanized (GI) CP1200. The chemical composition of the two steels is shown in table I.

Table II: Chemical compositions by weight percent of TBF1180 and CP1200 (Hausmann, 2014).

Steel	C	Si+Cr	Mn+Mo	Nb	P	S	N
TBF1180	0.17-0.22	1.0-1.4	2.3-2.7	<0.05	<0.01	<0.01	<0.007
CP1200	0.18-0.2	0.25-0.8	1.6-2.2	-	-	-	-

Two different dog bone tensile sample geometries were used. For the ductility trough testing, EG TBF1180 samples were 1.34mm thick, EG CP1200 samples were 1.19mm thick, and GI CP1200 samples were 1.52mm thick and all three used the geometry shown in Figure 5. For the small strain testing the same geometry samples were used for the EG CP1200, while the TBF1180 and the GI CP1200 were 1.5mm thick and used the geometry shown in Figure 6. All dimensions in the schematics below are in millimeters.

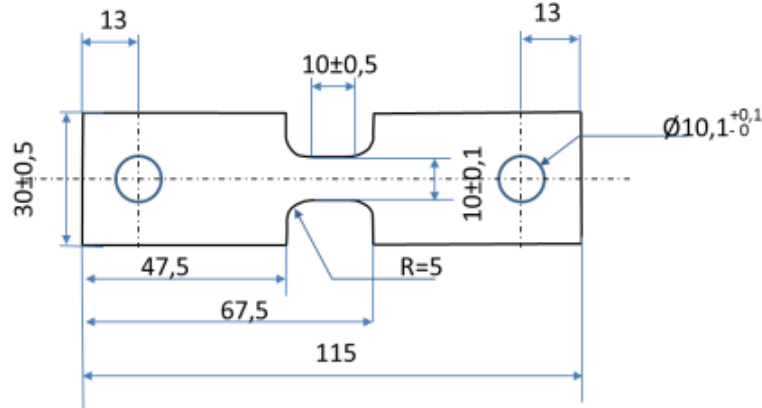


Figure 5. Geometry of the sample used for small strain testing of EG CP1200 and ductility trough testing of all steels

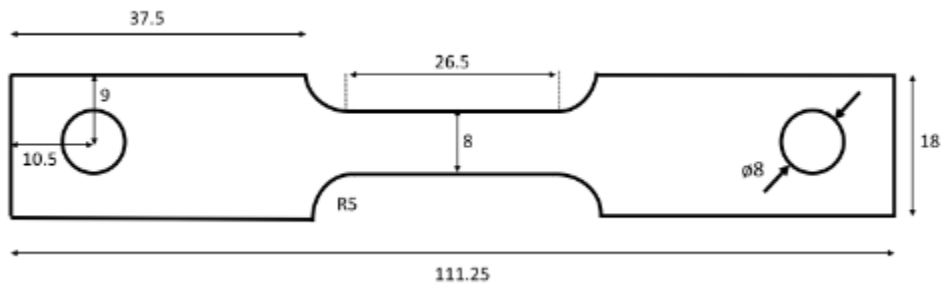


Figure 6. Geometry of the EG TBF1180 and GI CP1200 sample used for small strain testing

Three methods of sample preparation were used for the testing performed in this thesis. For the creation of all bare, zinc-free samples the galvanized dog bones were immersed in an acidic solution of one-part water, two-parts 37% hydrochloric acid, and 2g/L of hexamethylenetetramine for two minutes to dissolve all zinc present on the surface of the sample. The zinc coated samples for ductility trough testing the methodology of an industrial round robin was followed. In this, acid-resistant masking tape is applied to one side of the gauge section of the tensile dog bone and the same zinc dissolution procedure was then followed leaving zinc only in the area covered by the tape. This allowed thermocouples to be welded to the zinc-free side of the gauge section. The third method, which was used for the zinc coated

samples in the small strain experiments, involves sanding the zinc layer off of a small portion of the gauge length for thermocouple welding and leaving the rest of the zinc coating intact.

For the hot tensile testing in the Gleeble thermomechanical tester, copper grips stabilized by U-clamps applied the load and conducted the current which provided resistive heating to the sample. K-type thermocouples were spot welded to the center of the flat side of the sample and a ceramic sleeve was placed over the wires to prevent shorting. For the ductility trough testing a 39050 Jaw to Jaw L-Strain extensometer was used to measure displacement and calculate strain. For small strain testing an HZT071 extensometer was used to measure displacement and calculate strain. It was held to the sample using ceramic fiber cords tensioned by spring tabs. Figure 7 shows the testing setup for ductility trough testing and Figure 8 shows the setup for small strain testing.

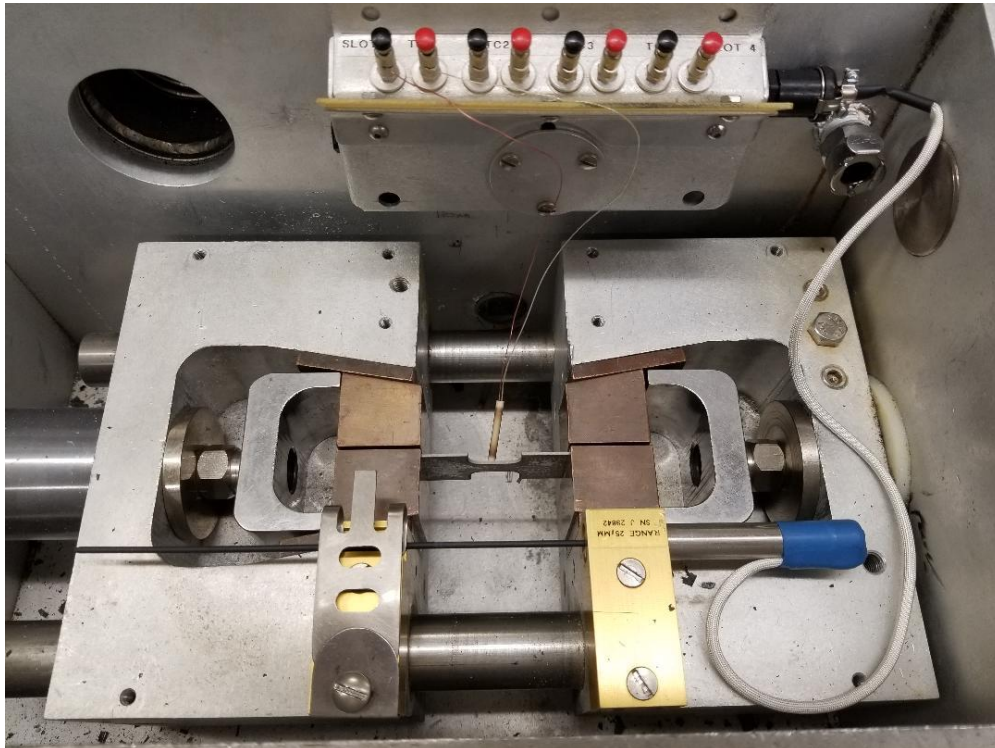


Figure 7. Experimental setup for ductility trough Gleeble hot-tension testing

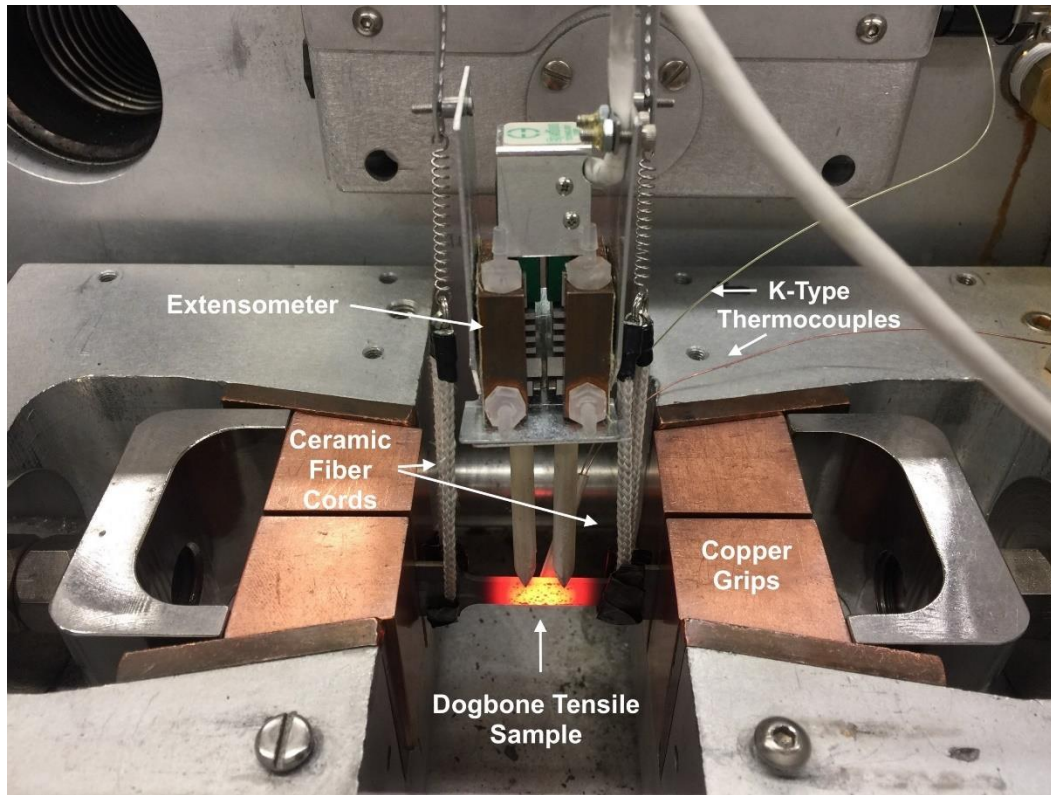


Figure 8. Experimental setup for small strain Gleeble hot-tension testing (Briant, 2018)

The Gleeble 1500D thermomechanical tester is used to generate the hot-tensile data for the samples. QuickSim2 software is used to program the Gleeble thermomechanical tester. In the ductility trough experiments uniaxial testing is performed at a range of temperatures from 600 °C to 1000 °C at 50 °C intervals. During heating, zero-force control is used, allowing the samples to expand freely and remove any load from thermal expansion. Once the target temperature is reached, all instrumentation is zeroed, removing the effect of heating from the stress-strain curves. Following the procedure of an industrial round robin a nominal strain rate of 0.3 strain per second is applied. The samples are pulled uniaxially until fracture occurs.

In the small total strain experiments uniaxial tensile testing is performed at 600 °C and 800 °C. During heating, zero-force control is used, allowing the samples to expand freely and remove any load from thermal expansion. Once the target temperature is reached, all

instrumentation is zeroed, removing the effect of heating from the stress-strain curves. The nominal strain rate chosen was 0.13 strain per second. Once the target temperature is reached, samples are pulled to nominal displacements of 0.1, 0.2, and 0.3mm under stroke displacement control. The samples are then held to cool. Figure 9 shows an example of the thermomechanical cycle for a small strain test.

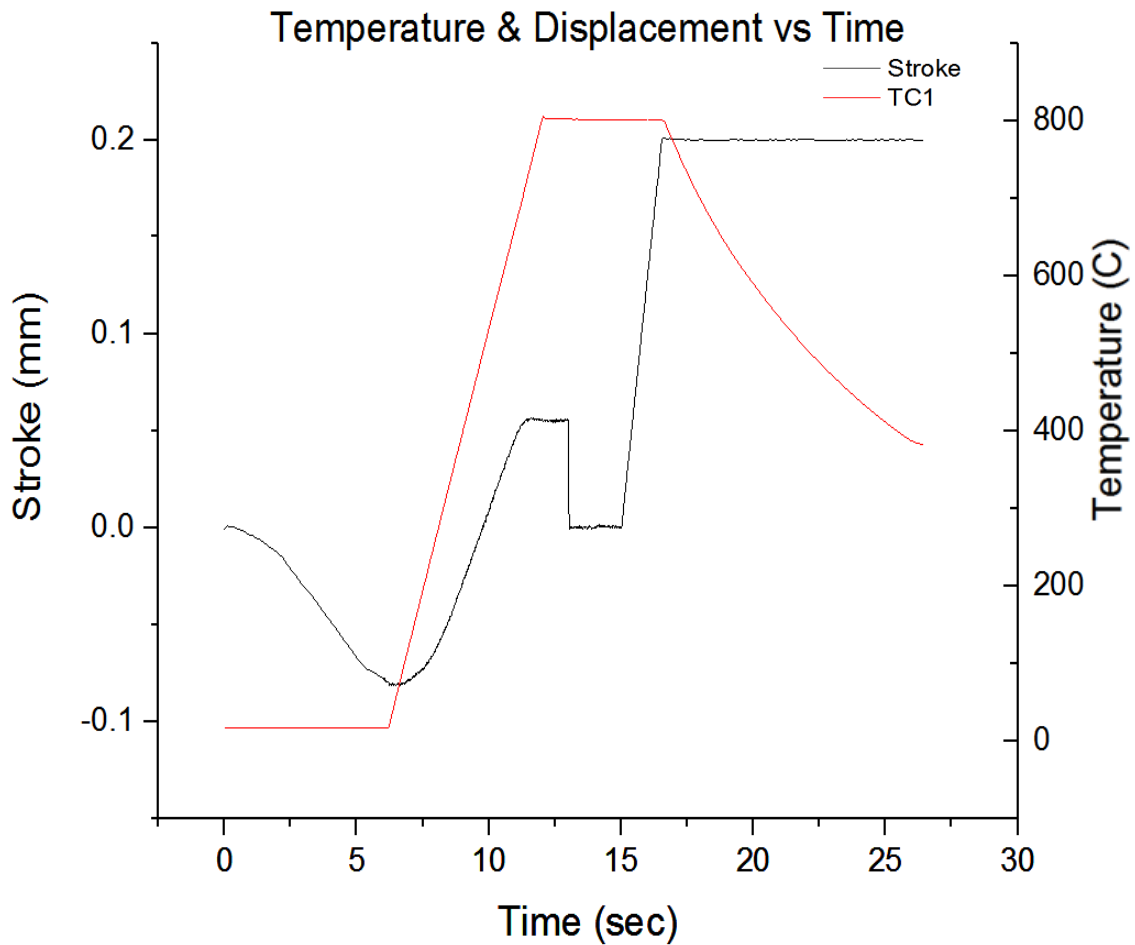


Figure 9. Example thermomechanical cycle for 0.2mm displacement test at 800 °C

After testing, small strain samples are prepared for scanning electron microscopy (SEM). This is done by first cutting the gauge section of the tensile sample from the grips and then cross-sectioning it lengthwise using a water-cooled cutoff saw. The samples are then mounted in

PolyFast resin. Polishing operations are performed using the PACE Technologies Nano 1000-T Manual Polisher. Grinding operations are performed using silicon carbide grit paper starting at 240 grit and finishing at 2000 grit. Polishing operations are performed first using 3-micron diamond suspension and finished with 1-micron diamond suspension. SEM images are taken with a TESCAN LYRA3 FIB-FESEM. Both secondary electron (SE) and back-scatter electron (BSE) images are taken. The working distance is 10mm and an accelerating voltage of 20 keV is used. Additionally, SEM fractography is performed on select samples from the ductility trough tests. This is performed with accelerating voltages of 5 keV and 20 keV and working distances ranging from 18mm to 25mm.

RESULTS

Ductility Trough Testing

By examining the fracture strain results of the different materials, it is seen that the type of AHSS and the method of galvanization affect the temperature range and severity of the LME response. It should be noted that each data point represents one sample. Figure 10 shows the ductility trough results of testing EG TBF1180 from 600 °C to 1000 °C. The blue points show the behavior of the control sample with all of the Zn coating removed prior to testing. The strain to fracture does not show a significant temperature dependence and ranges from 0.27-0.35 strain to fracture. In contrast the Zn-coated sample (orange dots) exhibits a strong temperature dependence with a range of fracture strains from 0.02 to 0.35. It should be noted that 1000 °C is well above the vaporization point of Zn (907 °C). As such, no Zn coating is expected to remain and the fracture strain for the two specimen types converge. From this figure it can be seen that EG TBF1180 experiences a strong LME response over a large range of temperatures. This is confirmed by the presence of intergranular fracture surfaces in the SEM images of the 600 °C sample. These images are shown in Figure 11. The low magnification image of the fracture surface of the 600 °C sample (Figure 11a) shows that the half of the sample where the zinc was removed necked and seemingly experienced ductile deformation, while the half of the sample with the zinc coating intact shows no necking and was seemingly brittle. This idea confirmed by the high magnification image (Figure 11b) as both micro-voids, an indicator of ductile failure, and grain facets, an indicator of brittle intergranular fracture, can be observed.

The fracture surface of the 800 °C sample of EG TBF1180 is shown in Figure 12. The low magnification image (Figure 12a) shows no noticeable necking which would suggest brittle fracture. This idea is furthered by the high magnification image (Figure 12b) which shows the faceted structure typical of brittle intergranular fracture.

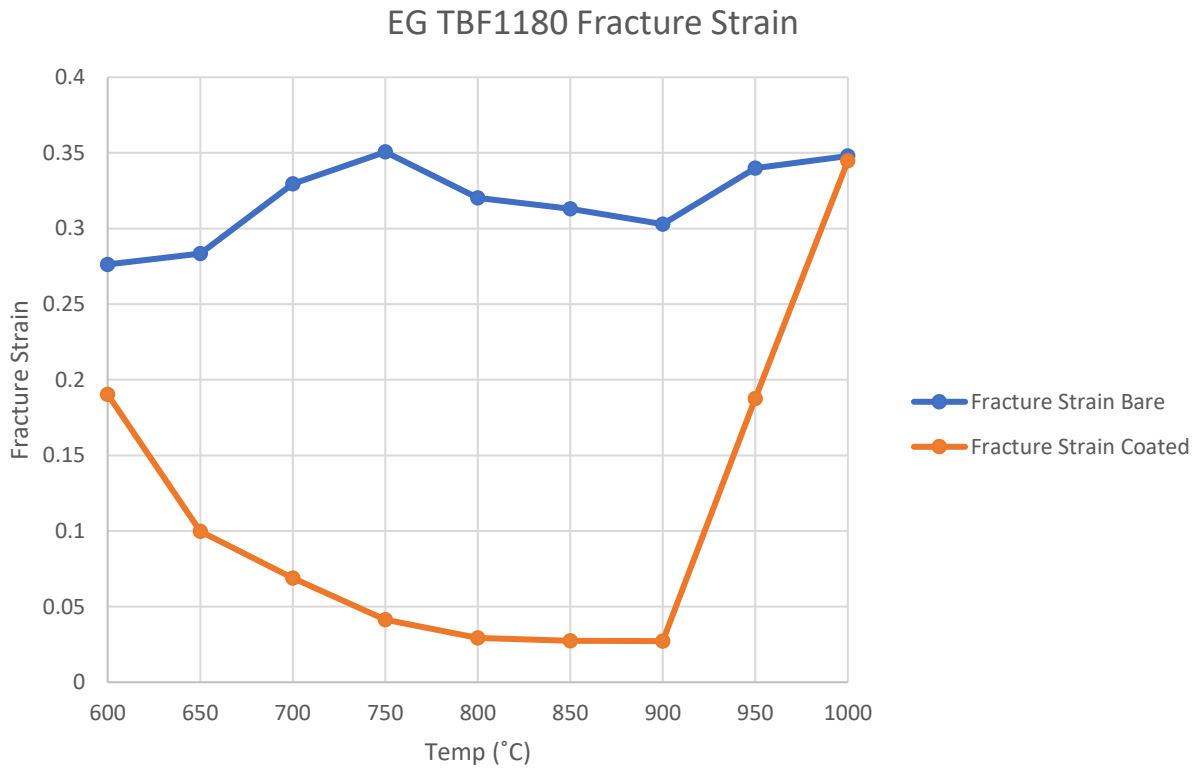


Figure 10. Temperature effect on ductility as measured by fracture strain for EG TBF1180

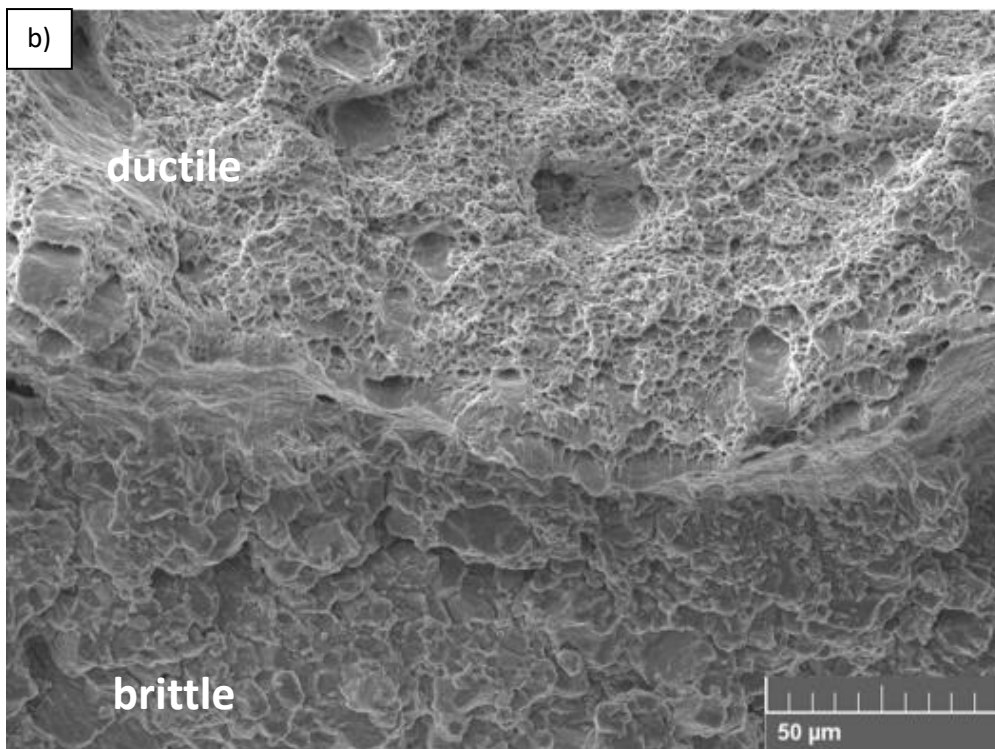
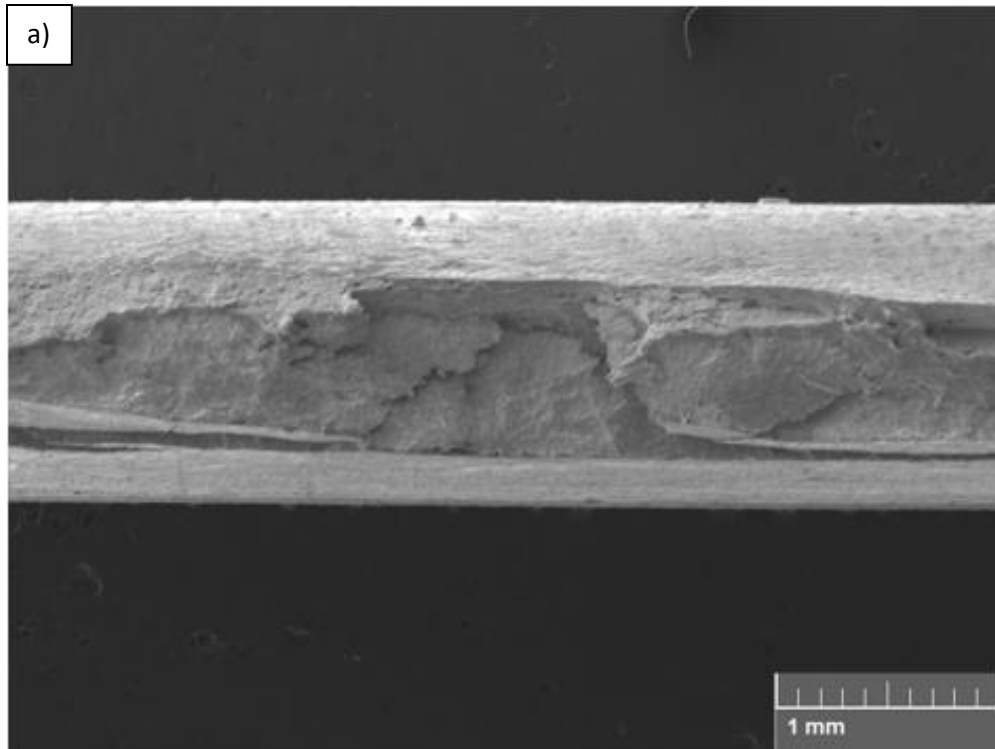


Figure 11. SE images of the fracture surface of EG TBF1180 at 600 °C showing brittle intergranular fracture on half of the sample (a) low magnification (b) high magnification

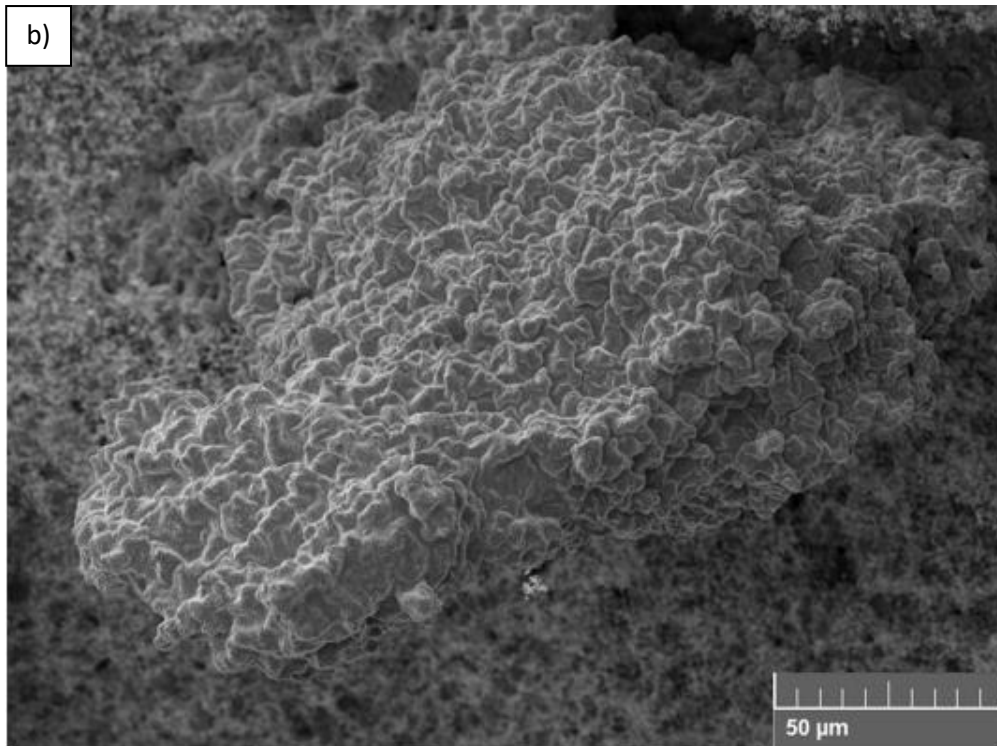
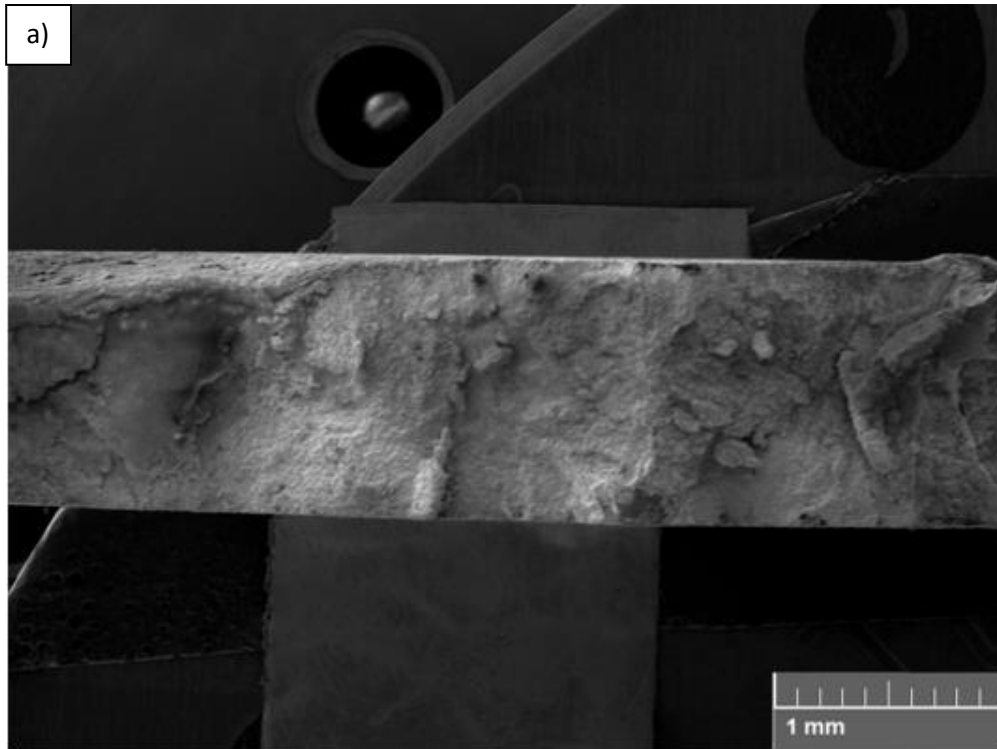


Figure 12. SE images of the fracture surface of EG TBF1180 at 800 °C showing brittle intergranular fracture through the sample (a) low magnification (b) high magnification

The ductility trough testing of EG CP1200 shows a much more narrowed temperature range for the LME response when compared to EG TBF1180, as there is only a large drop in ductility centered at 800 °C. There is a slight drop in ductility at lower temperatures, though not as significant as that seen in EG TBF1180. Interestingly, the ductility values for the zinc-coated samples at temperatures greater than 900 °C actually exceed those of the bare tests, though this is likely a result of experimental scatter indicating no loss of ductility as seen in EG TBF1180. The ductility trough results are graphed in Figure 13.

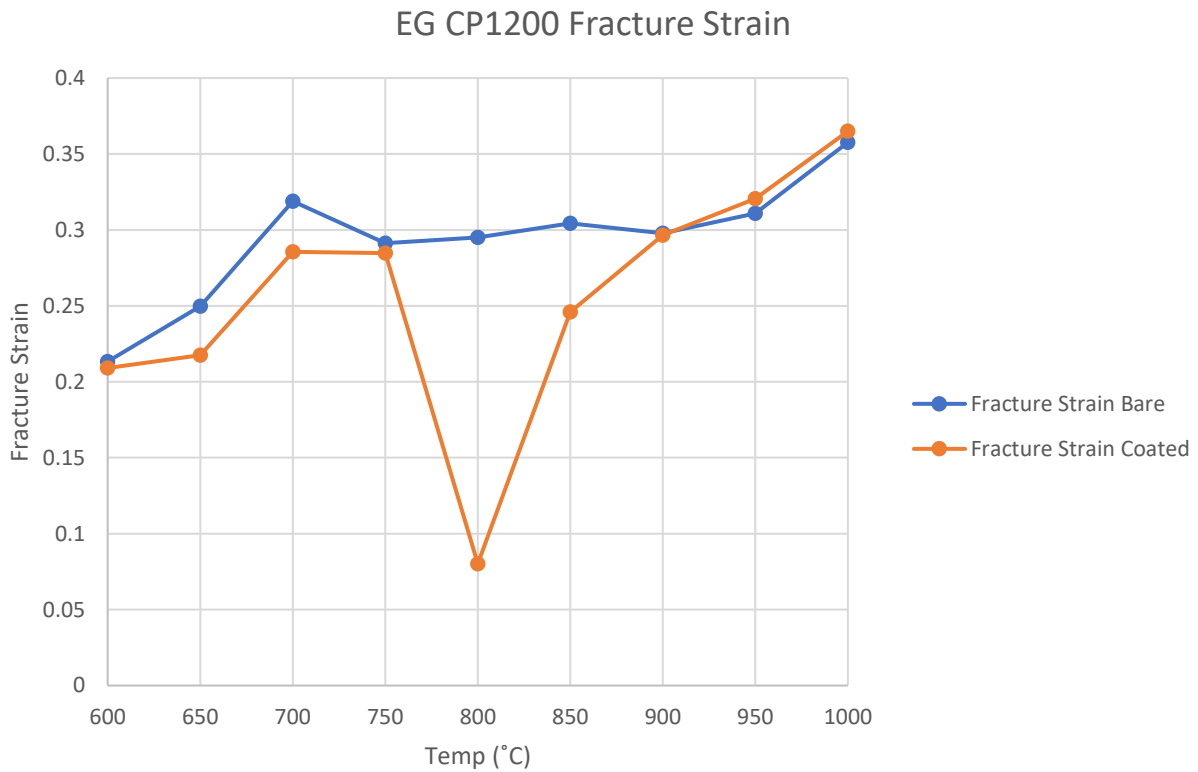


Figure 13. Temperature effect on ductility as measured by fracture strain for EG CP1200

Ductility trough testing of GI CP1200 indicates an LME response somewhere between that of EG CP1200 and EG TBF1180, but less severe. As seen in Figure 14, the ductility trough results show that GI CP1200 has a possible LME response over a range of temperatures (700 °C to 850 °C), which differs from EG CP1200 as that material only displayed a significant drop in

ductility at 800 °C. Additionally, while GI CP1200 loses ductility over a greater range of temperatures than EG CP1200 the loss of ductility is less severe. The differences between GI CP1200 and EG TBF1180 can be seen both the ductility trough graphs and with SEM fractography. The ductility trough plot of GI CP1200 shows that it does not share the same low temperature LME sensitivity as EG TBF1180. This is confirmed in the SEM images of the 600 °C sample of GI CP1200 shown in Figure 15, as this sample shows only the necking and microvoids indicative of ductile fracture whereas Figure 11 shows large areas of brittle fracture in EG TBF1180 at that temperature. Additionally, the ductility trough results show the GI CP1200 to have a less severe LME response than TBF1180 even at higher temperatures. Figure 16 provides more evidence for this, as the SEM images of the GI CP1200 show only half of the sample undergoing brittle intergranular fracture.

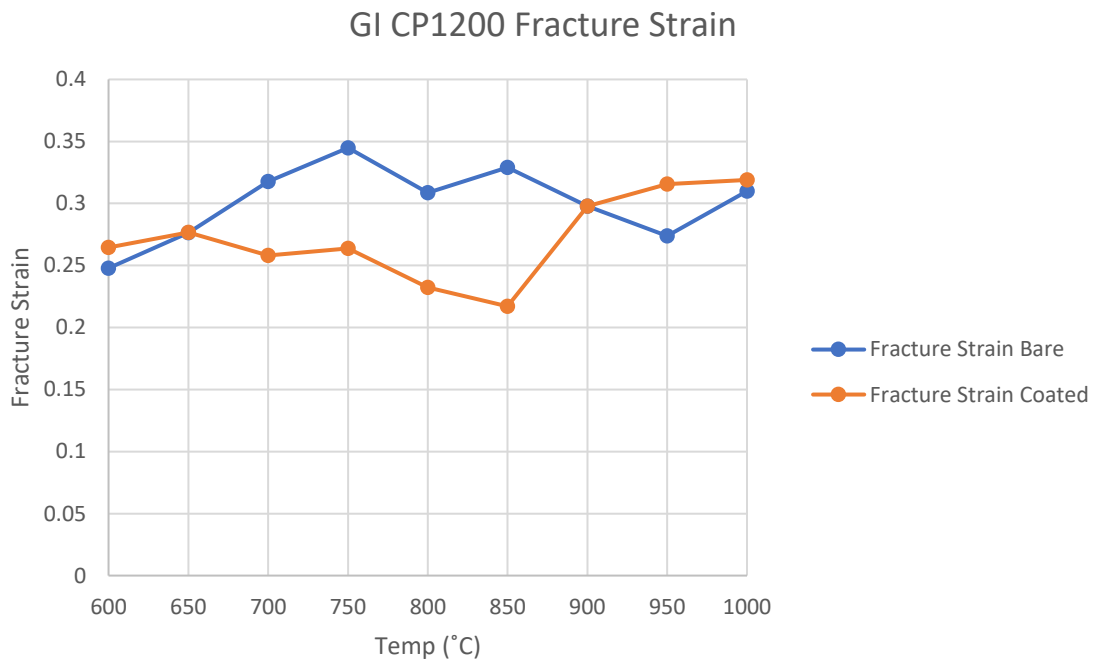


Figure 14. Temperature effect on ductility as measured by fracture strain for GI CP1200

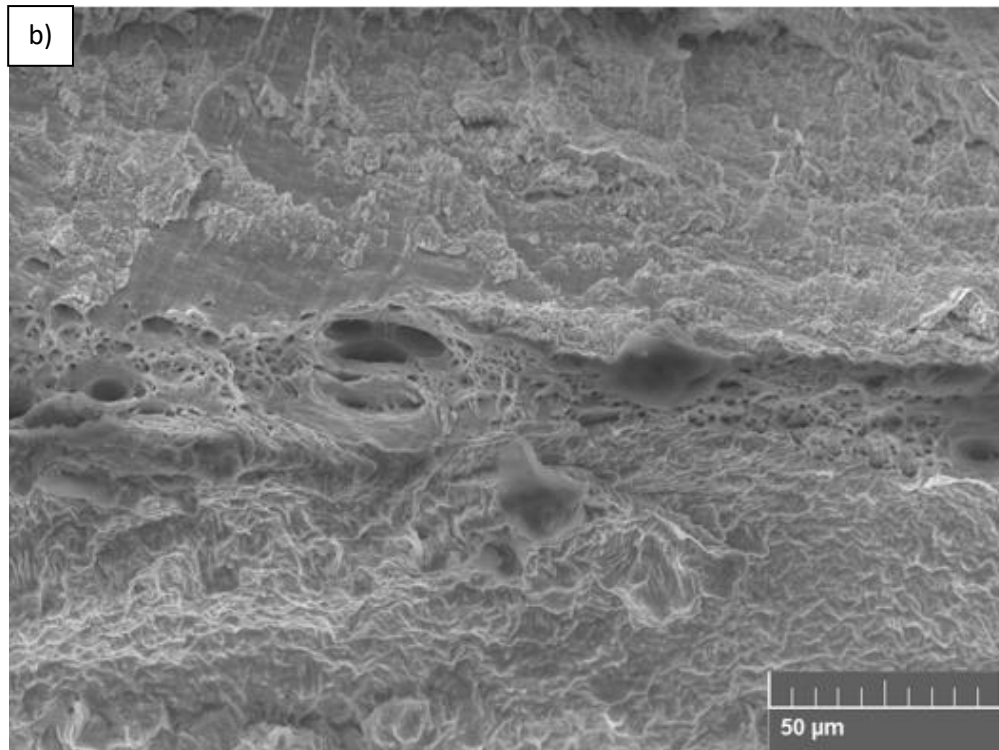
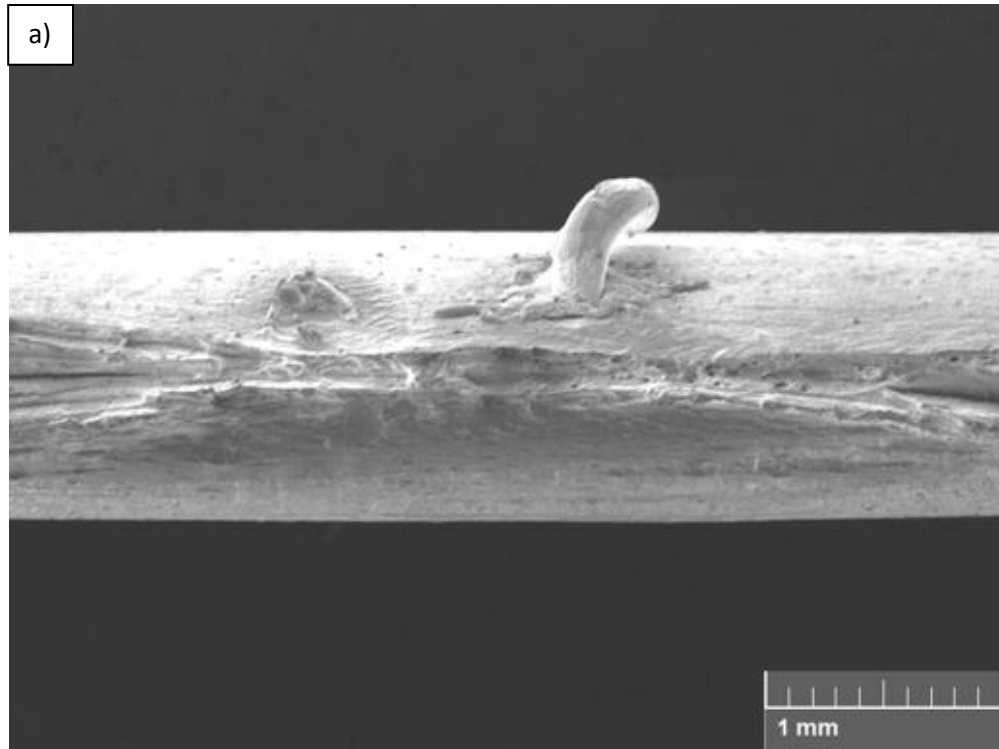


Figure 15. SE images of the fracture surface of GI CP1200 at 600 °C showing substantial necking (reduction in area) and micro-voids (a) low magnification (b) high magnification

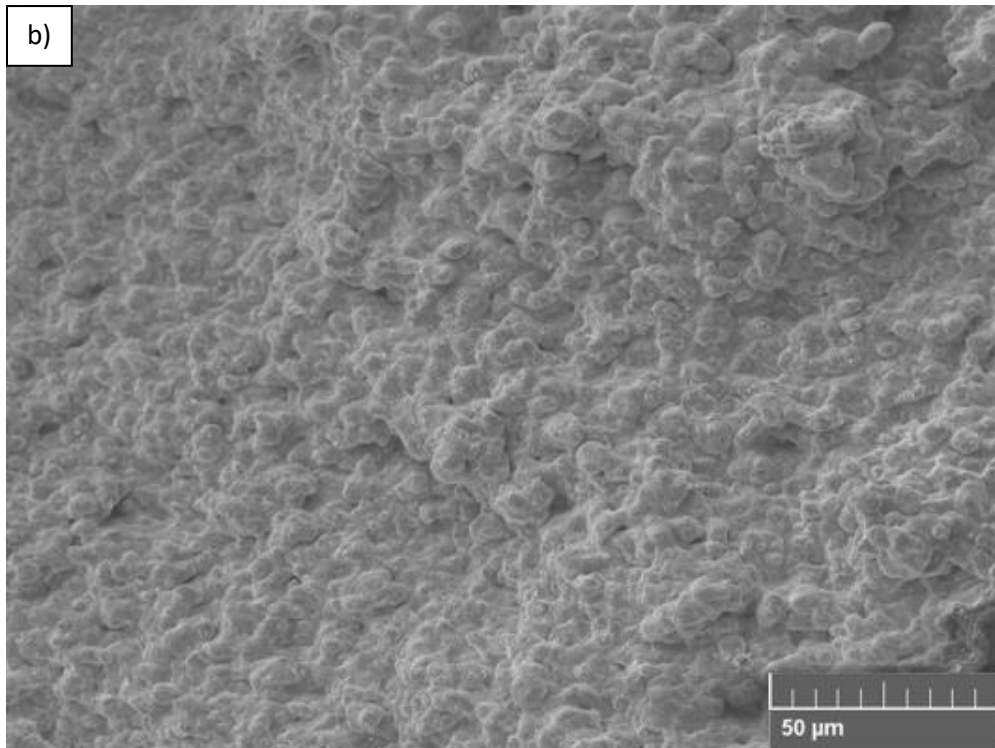
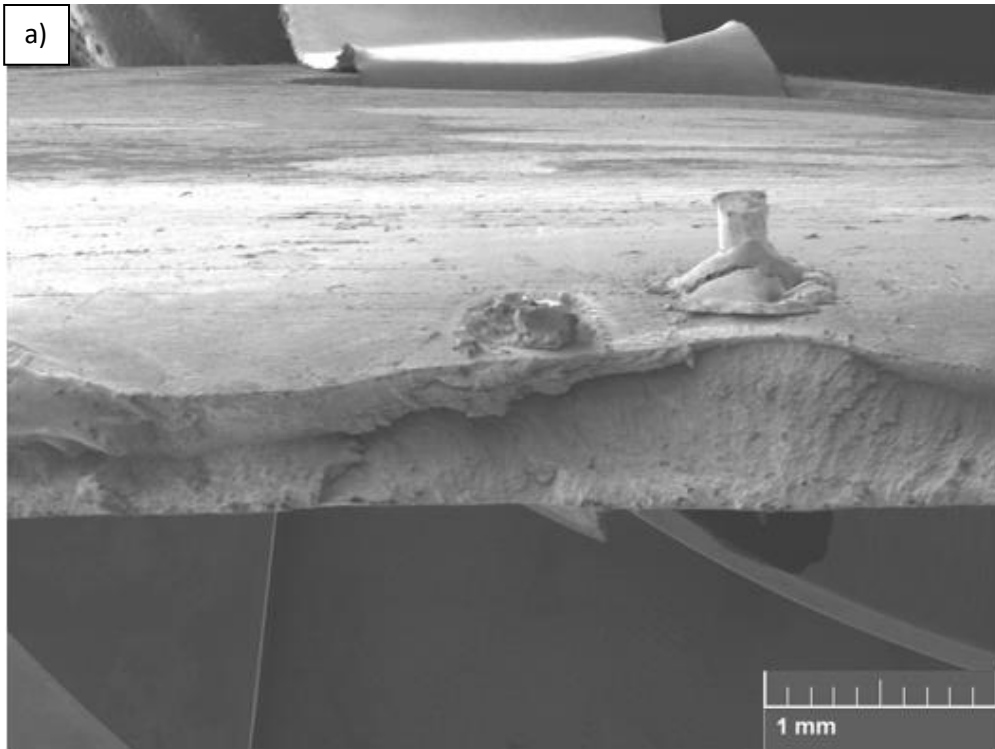


Figure 16. SE images of the fracture surface of GI CP1200 at 800 °C showing necking and brittle fracture in different areas (a) low magnification (b) high magnification

Small Strain Testing

As the small strain testing was conducted by the Gleeble during stroke-controlled testing, the macro-elastic or macro-plastic behavior of each small strain test had to be confirmed from the stress versus strain curves created. The Young's moduli for these materials were calculated from the linear portions of the small strain tensile curves and are tabulated alongside the high temperature Young's moduli of two steels with similar room temperature elastic moduli in Table III. From this it can be seen that the experimental Young's moduli fall within the established range for high strength steels. Observation of the 0.1mm displacement curves in Figures 17, 18, and 19 show that the curve remains in the linear, elastic strain region. Additionally, plotting the Young's modulus line with the 0.2% plastic strain offset for GI CP1200 at 800 °C, as shown in Figure 20, shows the 0.1mm pull ends before the engineering yield point. It holds true that for all materials and all temperatures tested the maximum strain value of the 0.1mm pull never exceeds the 0.2% strain threshold that defines engineering plastic yield strain, at least in a macroscale sense. Therefore the 0.1mm stroke tests can be treated as macro-elastic tests. Similarly, in all cases 0.3mm stroke test curves are clearly seen to exceed the plastic yield strain threshold and the tests can be treated as being macro-plastic for all conditions. The 0.2mm curves, however, show only slight plasticity in some cases and can be treated as an intermediate case.

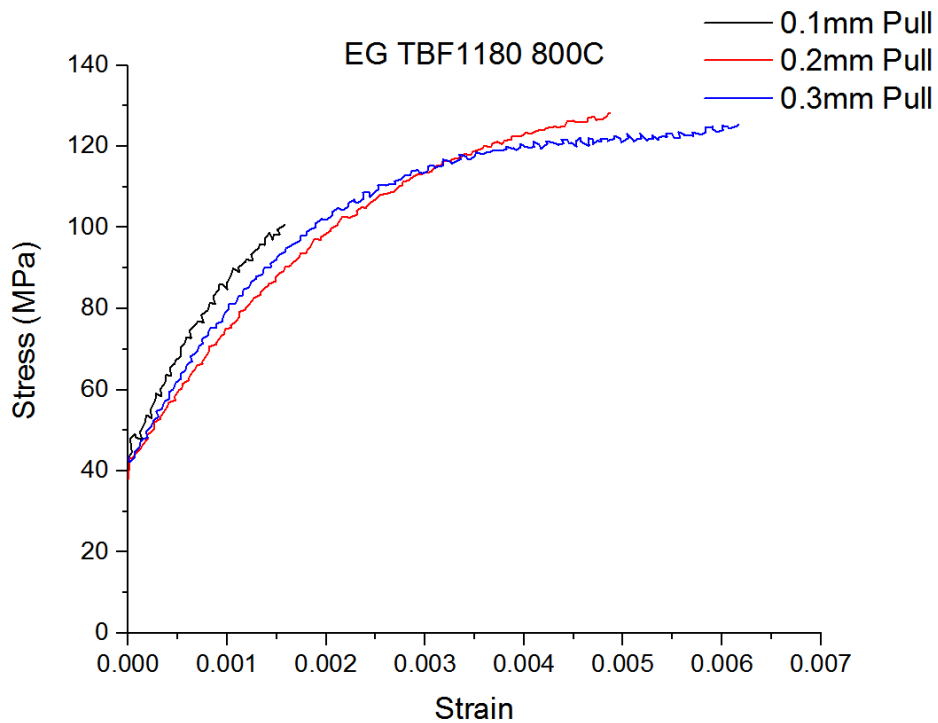
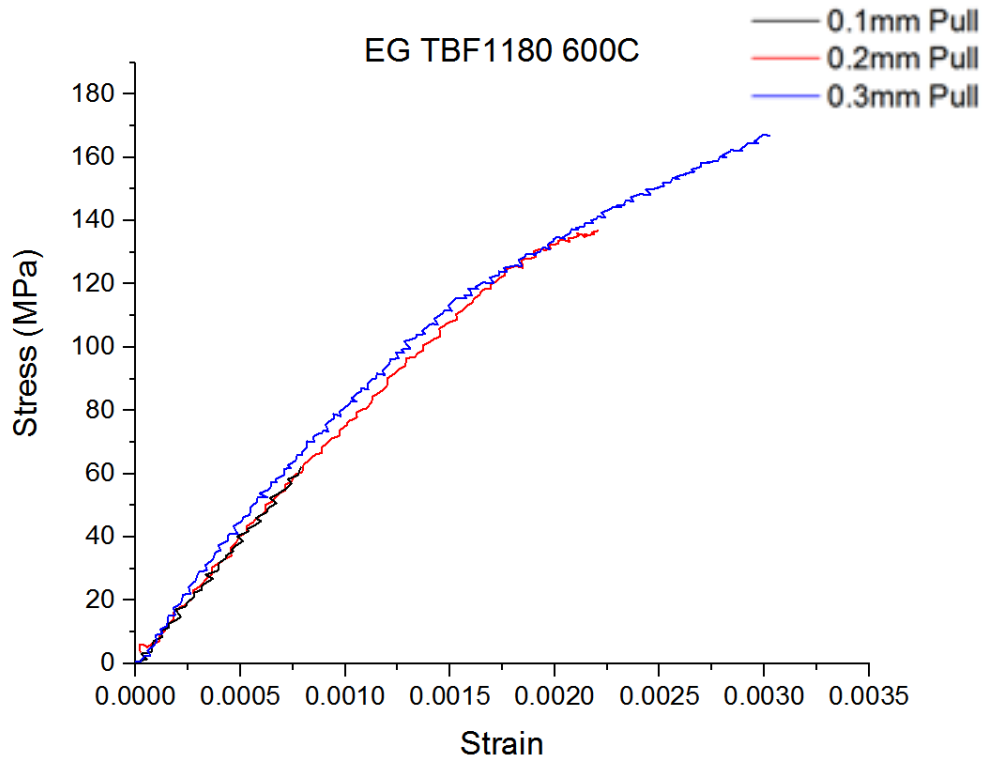


Figure 17. Small strain testing of EG TBF1180 (top) 600 °C (bottom) 800 °C

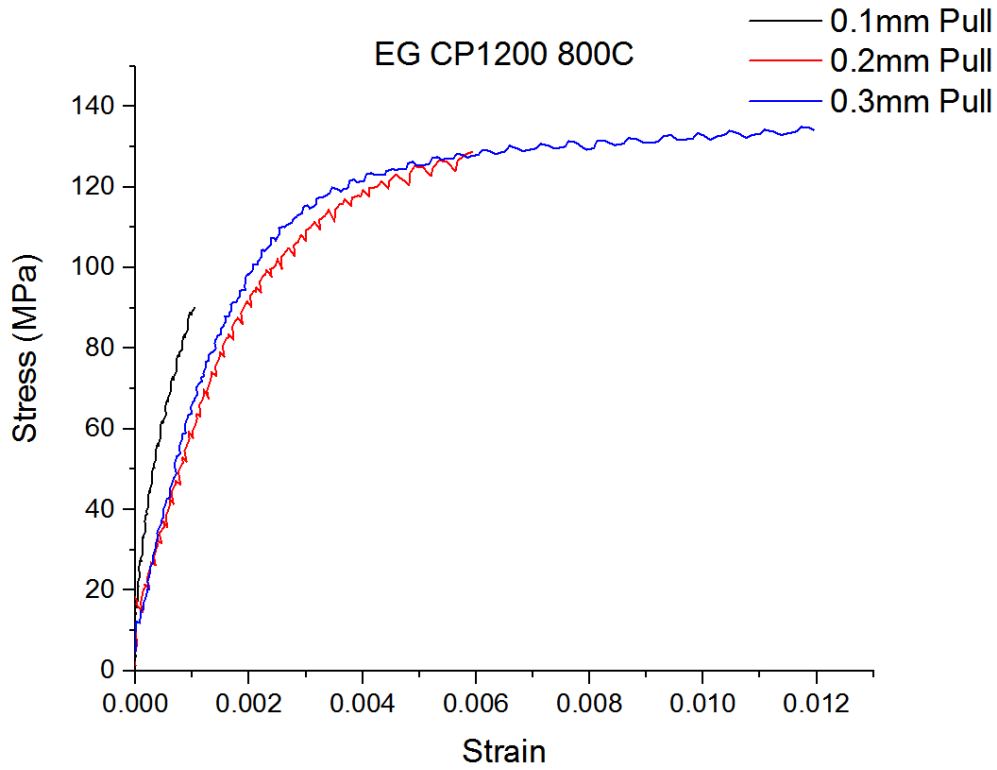
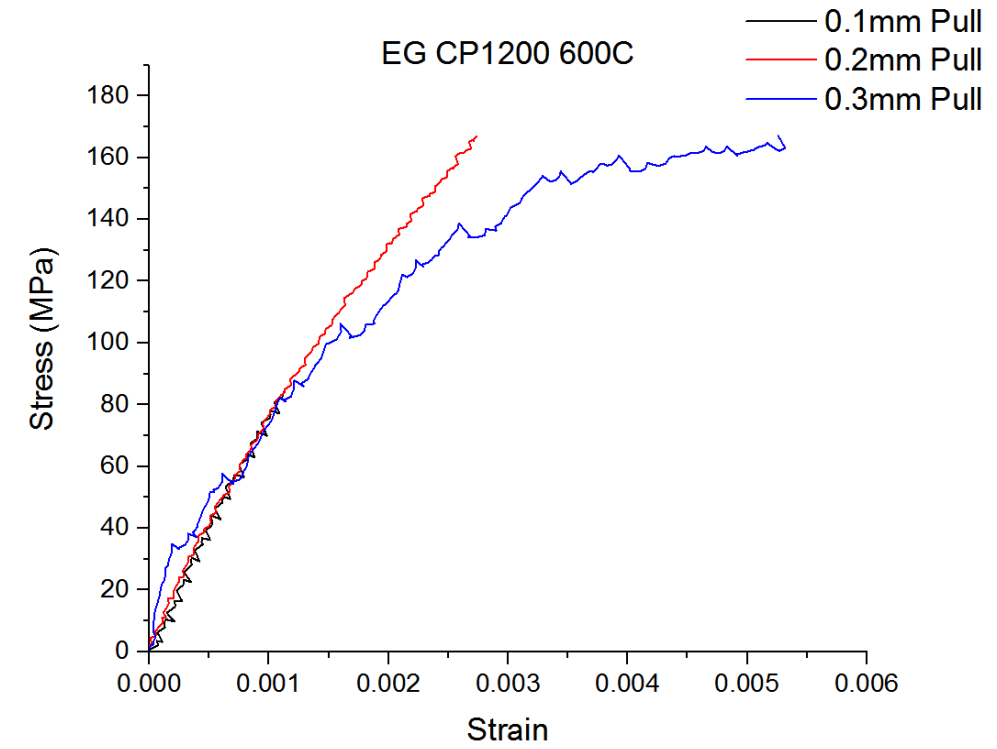


Figure 18. Small strain testing of EG CP1200 (top) 600 °C (bottom) 800 °C

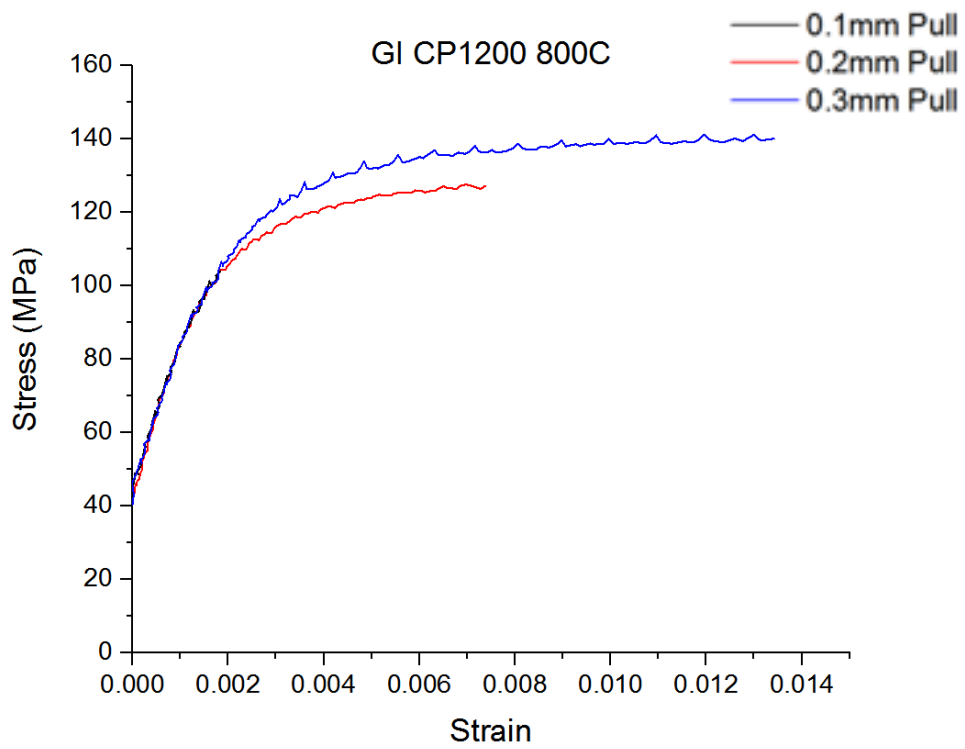
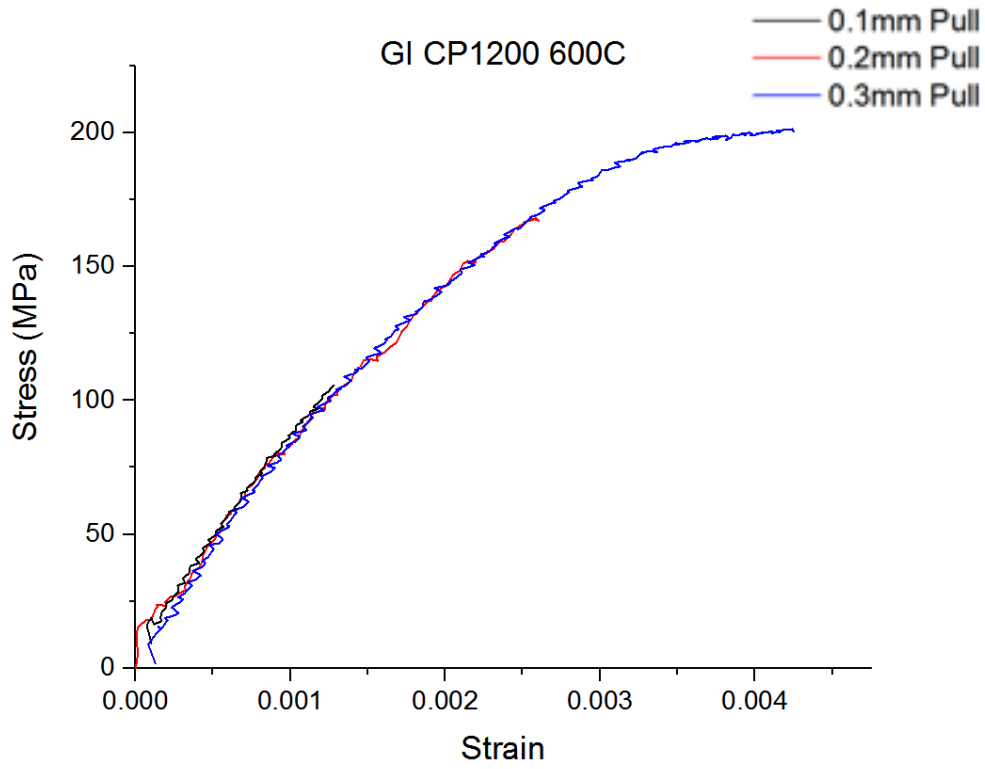


Figure 19. Small strain testing of GI CP1200 (top) 600 °C (bottom) 800 °C

Table III: Experimental Young's moduli at high temperature for TBF1180 and CP1200 compared with literature on Grade 22 steel and S355J2H structural steel (Grade 22, 2005) (Outinen & Mäkeläinen, 2002).

Experimental				
Material	Test	0.1mm	0.2mm	0.3mm
EG TBF1180	600C	78.6GPa	72.2GPa	76.3GPa
	800C	36GPa	31GPa	33.9GPa
EG CP1200	600C	76.4GPa	73.3GPa	73.3GPa
	800C	72.8 GPa	43.1GPa	47.3GPa
GI CP1200	600C	77.9GPa	71.9GPa	76.5GPa
	800C	32.9GPa	36.5GPa	35.8GPa
Literature				
Grade 22	600C	163.4GPa		
	800C	131GPa		
S355J2H	600C	65.1GPa		
	800C	18.9GPa		

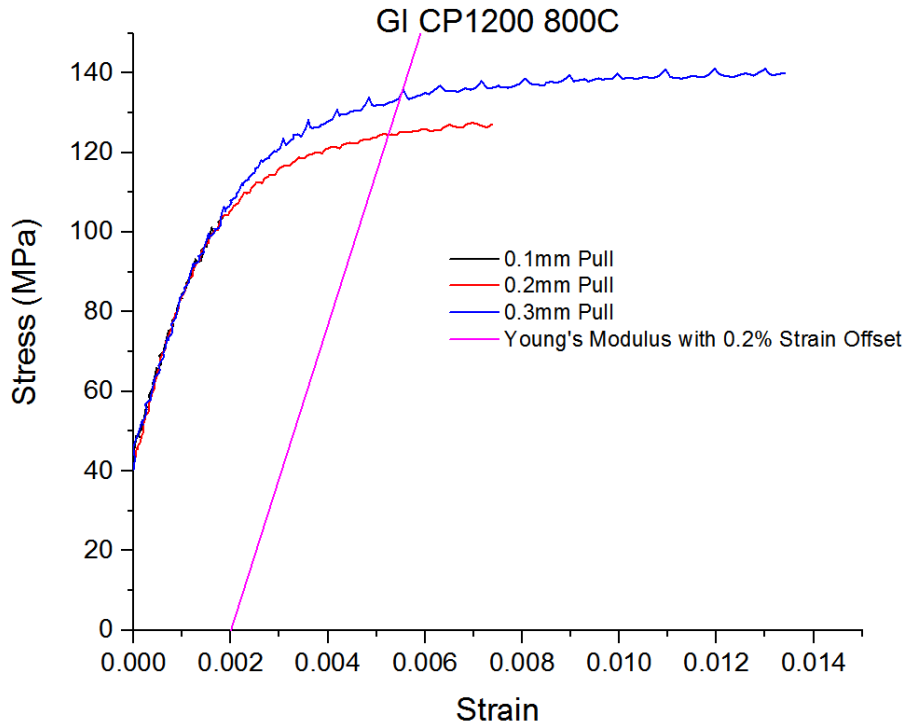


Figure 20. Stress strain curve of GI CP1200 with Young's modulus at 0.2% strain offset

When examining the cross-sections of the 0.3mm stroke test samples with BSE imaging, some similarities and differences between can be seen in the effect of the tests on the different materials. First, as can be seen in Figure 21, all the materials tested develop cracks at 800 °C. To address the potential influence of thermal stresses upon cooling, the hot tension test with 0.3 mm stroke was repeated for EG TBF1180 while allowing the sample to contract freely (zero load condition) as it cooled. No notable difference was observed in the small cracks formed (Figure 21a vs Figure 21b). The severity of the cracking, however, differs among the samples. When comparing the two electro-galvanized steels, the EG TBF1180 (Figure 21b) shows a greater number of cracks in its surface than the EG CP1200 (Figure 21d). Additionally, a starker difference can be seen between the surfaces of the two CP1200 samples. The hot-dip galvanized sample (Figure 21c) has many cracks of greater than 10µm in length running out from its zinc-steel interface, while the cracks in the electro-galvanized CP1200 (Figure 21d) are comparatively scarce and less than 2.5µm long. All of these cracks appear to match the structure expected from intergranular cracking. This increase in severity of cracking is counter to the results of the ductility trough experiments where EG CP1200 shows more severe LME behavior at 800 °C.

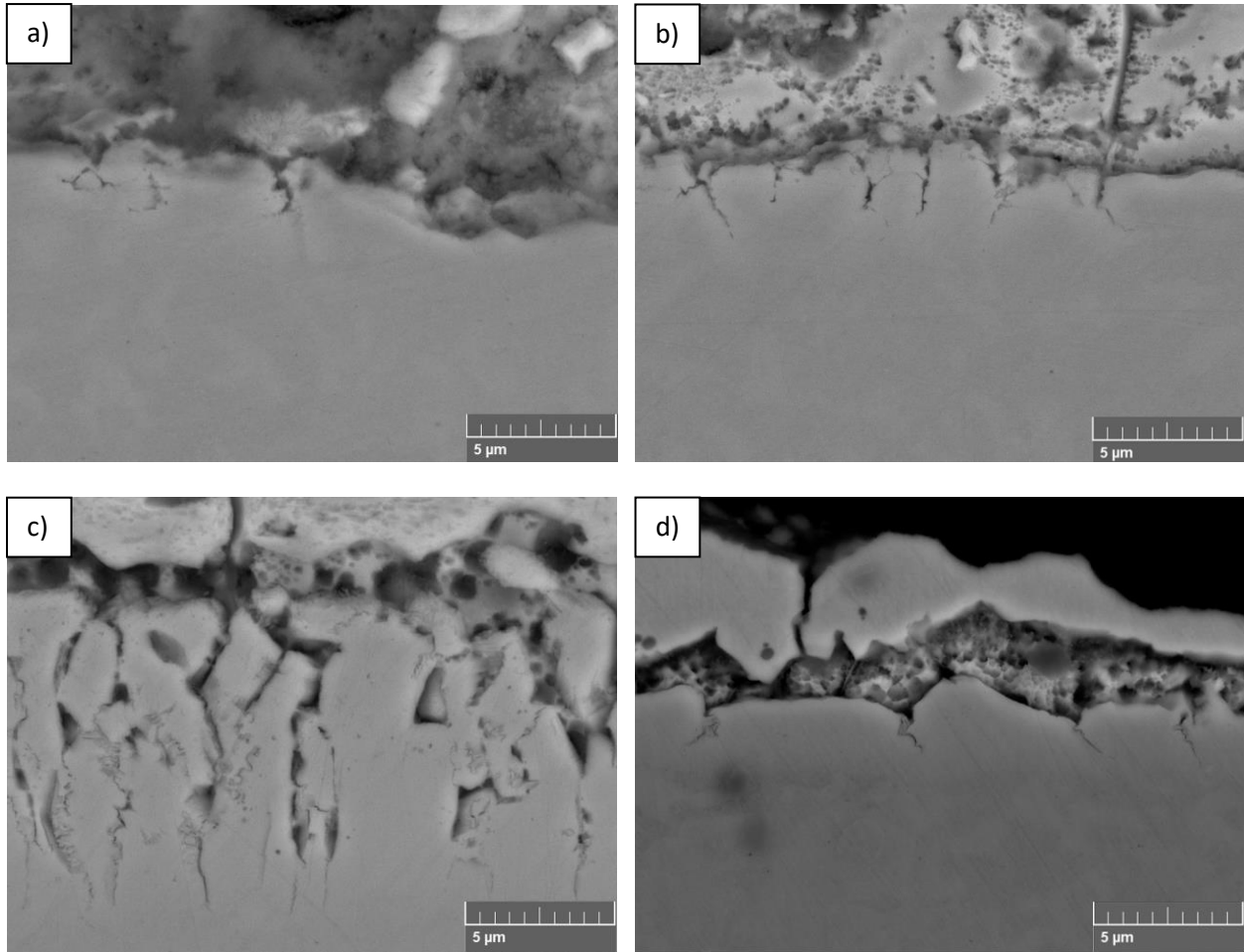


Figure 21. BSE images of the zinc-steel interface of 800 °C 0.3mm stroke test (a) EG TBF1180 0kN cooling (b) EG TBF1180 (c) GI CP1200 (d) EG CP1200

In the 600 °C 0.3mm stroke test there is a clear difference between the behavior of TBF1180 and CP1200. As shown in Figure 22 below, neither the EG CP1200 (Figure 22c) nor the GI CP1200 (Figure 22b) develop cracks under these testing conditions. The EG TBF1180 (Figure 22a) on the other hand does. A comparison of these cracks to those seen in the 800 °C 0.3mm sample (Figure 21b) show those in the 600 °C sample to be similar in size but lesser in number. This agrees with the results of the ductility trough tests as only EG TBF1180 showed significant LME behavior at 600 °C but it was less severe than at 800 °C (Figure 10).

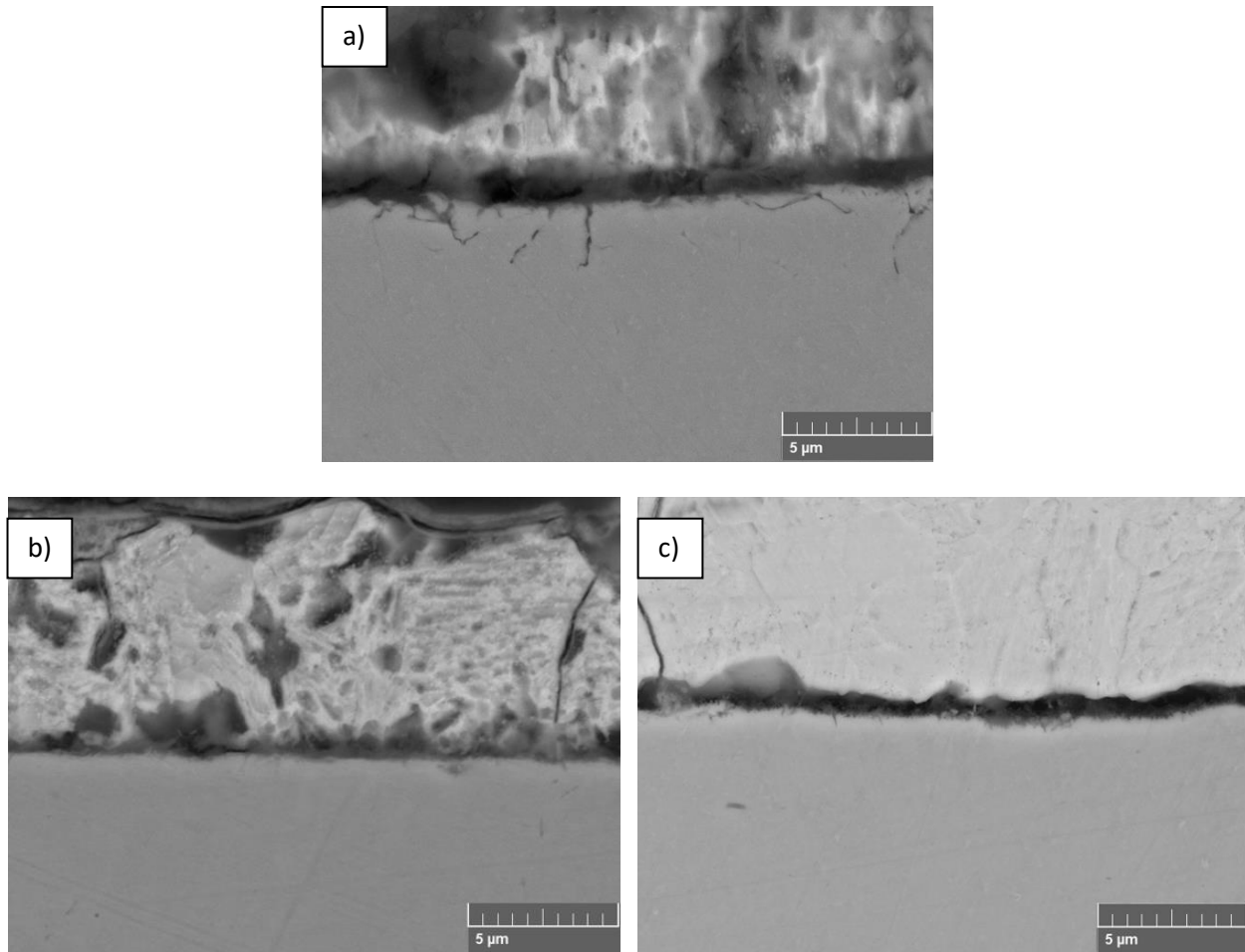


Figure 22. BSE images of the zinc-steel interface of 600 °C 0.3mm stroke test (a) EG TBF1180 (b) GI CP1200 (c) EG CP1200

The results of the 800 °C 0.2mm stroke test are similar to the results of the 800 °C 0.3mm stroke test. All three samples have cracks, but they are not equal in number or size as shown in Figure 23 below. While the EG TBF1180 (Figure 23a) and the EG CP1200 (Figure 23c) each have fewer than 5 cracks all of less than 5μm in length issuing from their respective zinc-steel interfaces, the surface of the GI CP1200 (Figure 23b) once again has more than a dozen cracks greater than 5μm in length. Continuing this trend, the results of the 600 °C 0.2mm stroke test echo the results of the 0.3mm test of the same temperature. Figure 24 shows that cracks have formed in the TBF1180 (Figure 24a) sample while both of the CP1200 samples remain free of cracks.

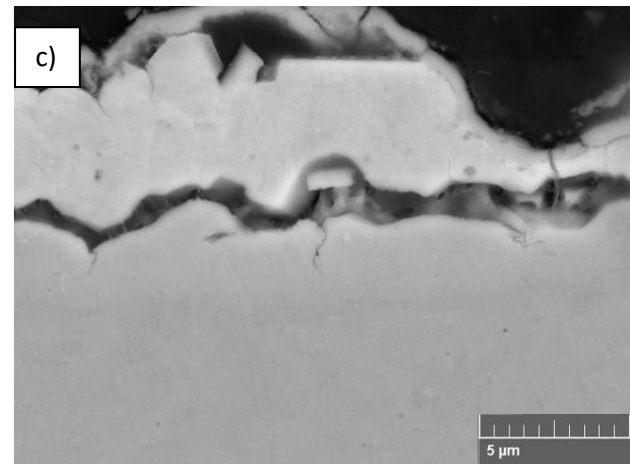
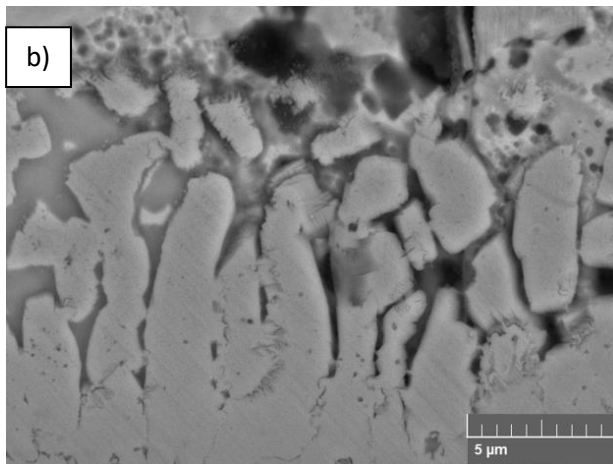
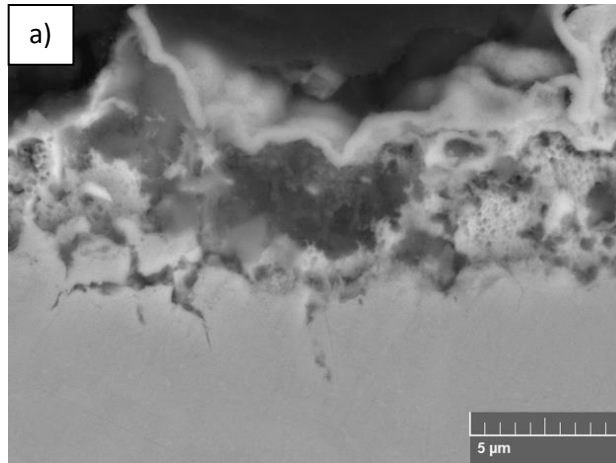


Figure 23. BSE images of the zinc-steel interface of 800 °C 0.2mm stroke test (a) EG TBF1180
(b) GI CP1200 (c) EG CP1200

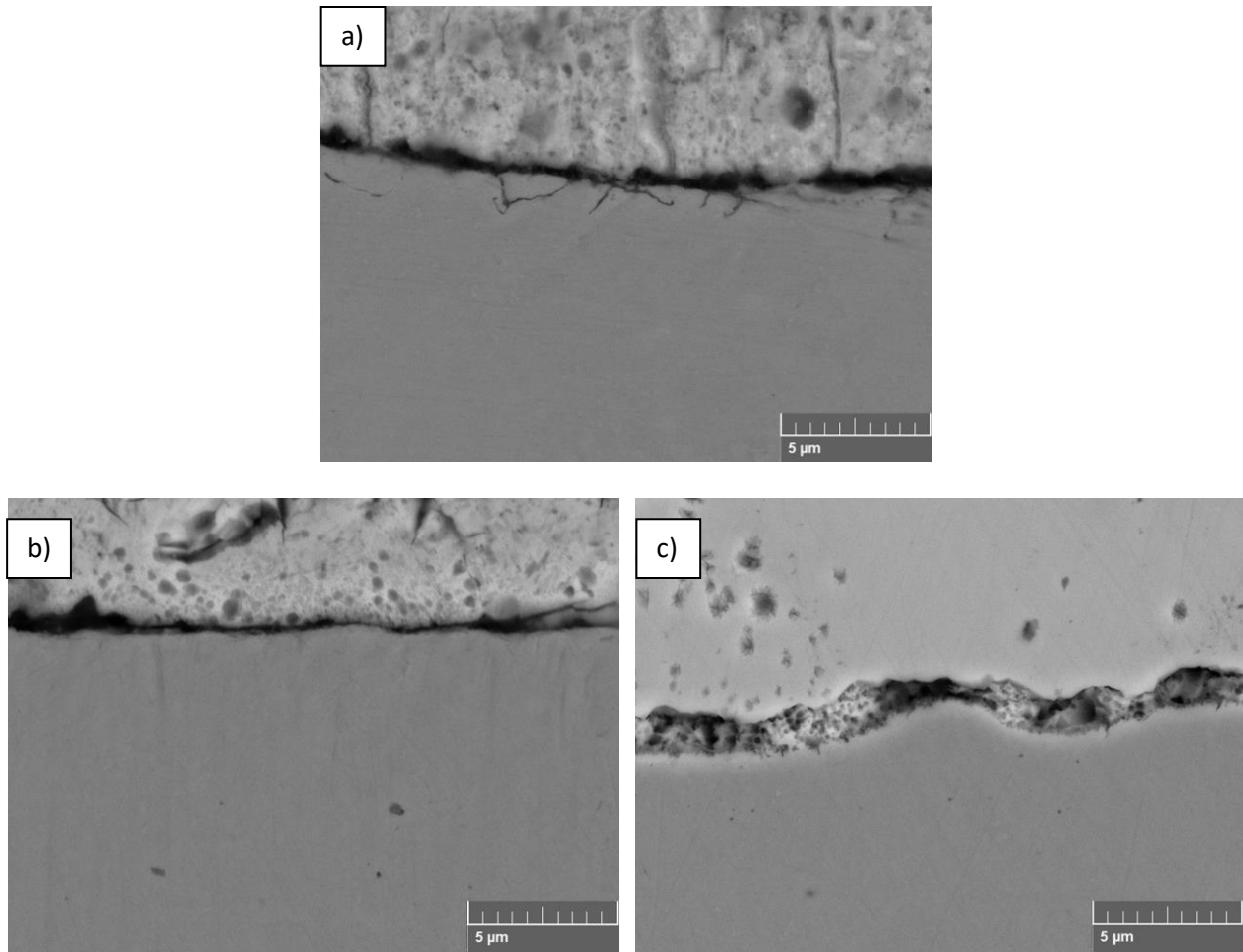


Figure 24. BSE images of the zinc-steel interface of 600 °C 0.2mm stroke test (a) EG TBF1180 (b) GI CP1200 (c) EG CP1200

The final sets of small total strain experiments are run to 0.1mm stroke and, as shown in the earlier graphs, represent a macro-elastic loading condition for the samples. As such it is important to note that at 800 °C all three materials: EG TBF1180, EG CP1200, and GI CP1200 form cracks as a result of testing. Of these, the cracks in the GI CP1200 are the most developed, and those in the EG CP1200 the least, with only one or two small cracks being visible. All three samples are shown in Figure 25. The 600 °C macro-elastic experiments yield the same results as the other 600 °C experiments, as the CP1200 samples do not nucleate cracks but the TBF1180 does. With the results in Figure 26, EG TBF1180 has been shown to crack under all temperature and strain conditions tested. Additionally, to ensure that these were in fact LME cracks, the

0.2mm 800 °C sample of GI CP1200 was examined using energy dispersive x-ray spectroscopy (EDS). With this technique it was found that the cracks were zinc-rich as would be expected from LME. These results are shown in Figure 27.

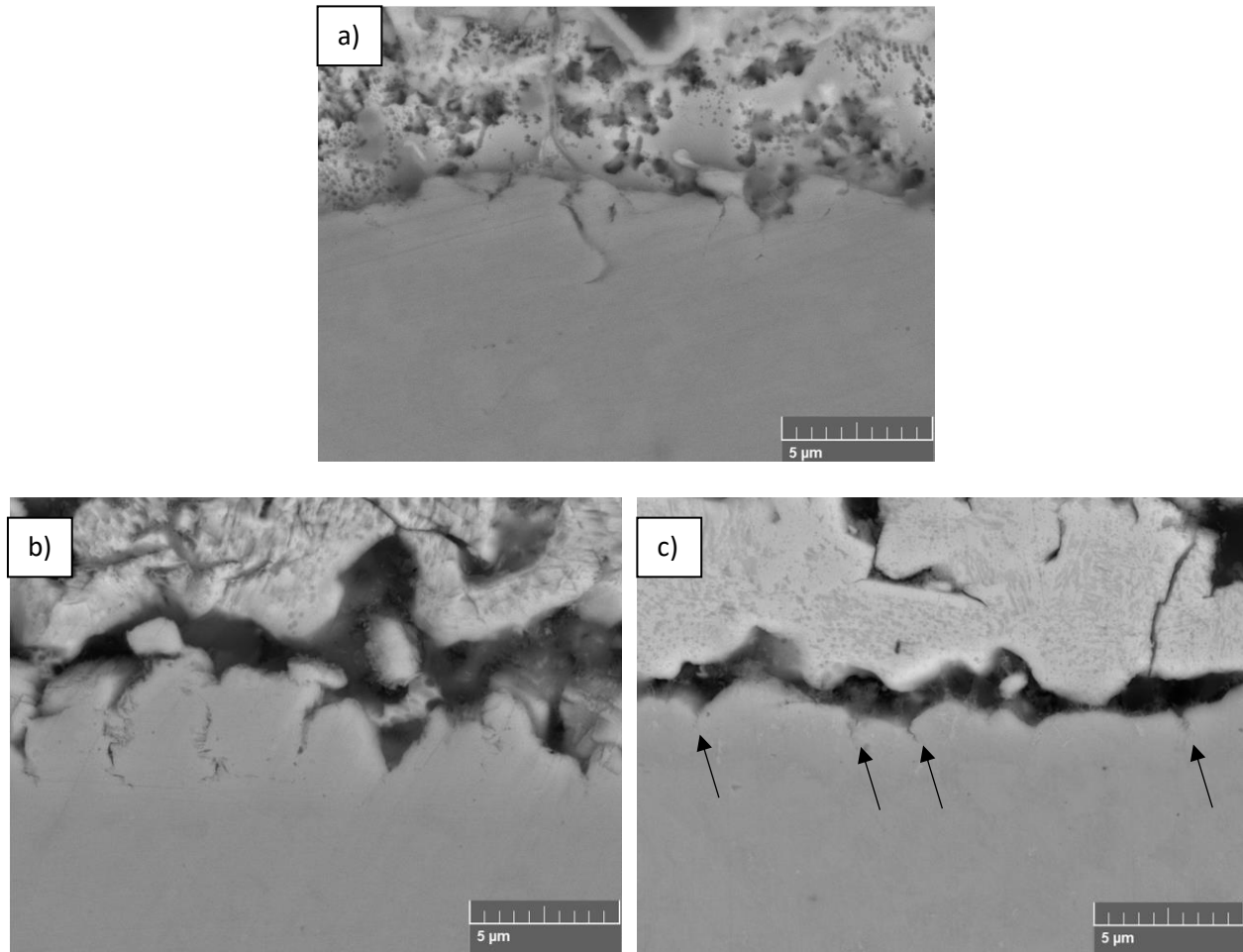


Figure 25. BSE images of the zinc-steel interface of 800 °C 0.1mm stroke test (a) EG TBF1180 (b) GI CP1200 (c) EG CP1200 (black arrows point to small cracks at the surface)

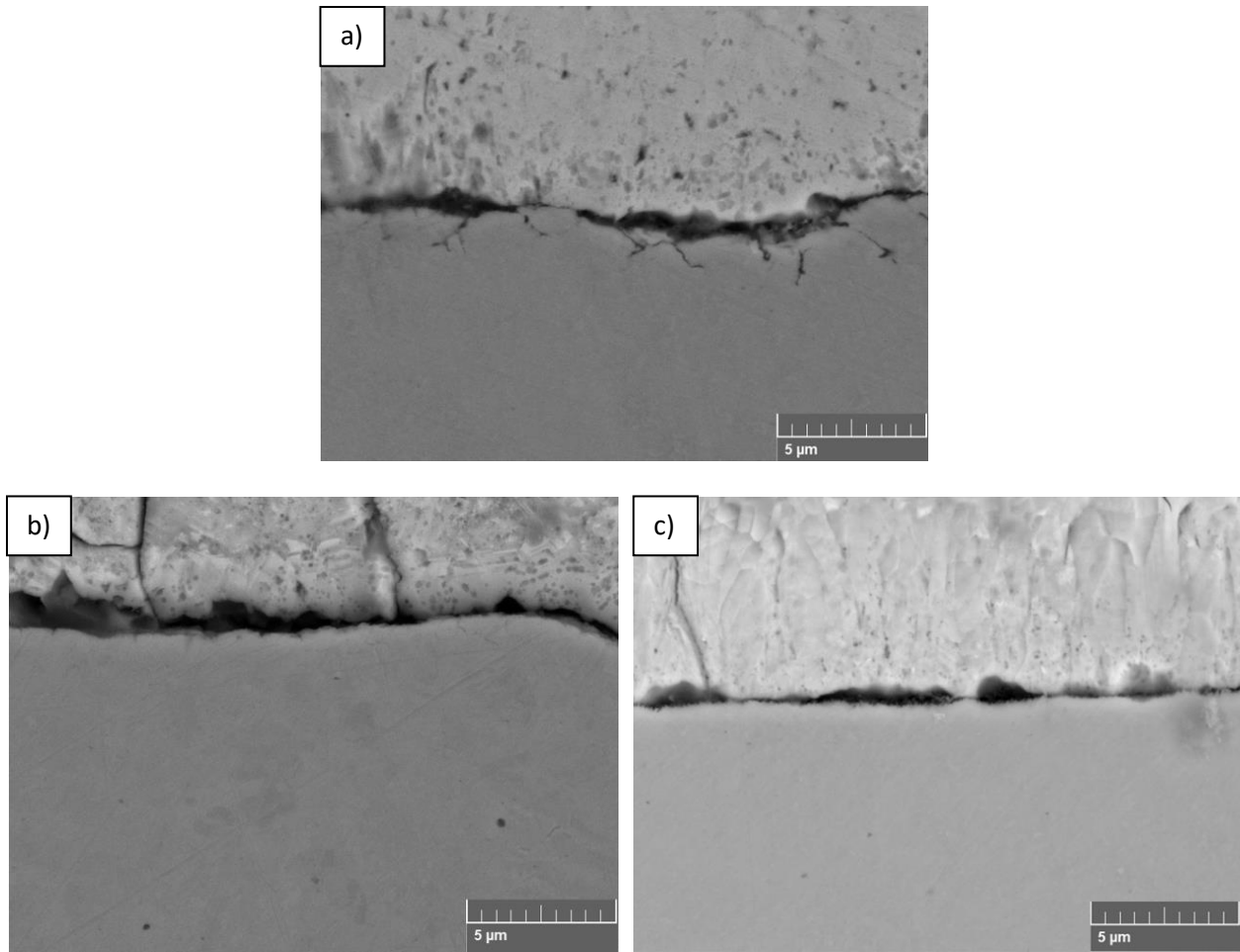


Figure 26. BSE images of the zinc-steel interface of 600 °C 0.1mm stroke test (a) EG TBF1180 (b) GI CP1200 (c) EG CP1200

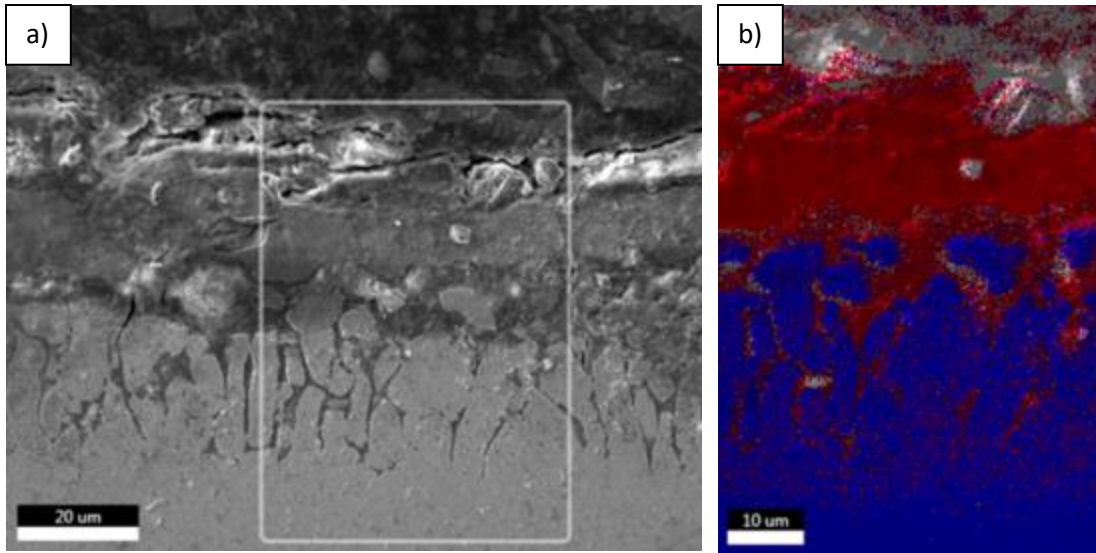


Figure 27. (a) BSE image of 0.2mm 800 °C GI CP1200 sample with white box indicating area examined with EDS (b) EDS results for this area with red indicating zinc-rich areas

DISCUSSION

This work demonstrates several things about LME. First, it can be seen that LME can occur at low macro-strain values, even those falling within the macro-elastic range. As seen in Figures 21 and 23 at 800 °C well-developed cracks matching the expected structure of those formed by LME are present in all materials tested after plastic deformation. Additionally, by examining Figures 17, 18, 19, and 25 it can be observed that macro-elastic testing is enough to produce LME cracks in sensitive materials at 800 °C. This can be concluded because for all three materials tested: EG TBF1180, EG CP1200, and GI CP1200, the measured strain of testing falls below the 0.2% strain threshold designated as the border between elastic and plastic deformation. Despite this, Figure 25 shows that all three materials experience crack nucleation and growth even at this limited, macro-elastic strain. It must be noted, however, that even at macro elastic strain values small-scale micro-plastic deformation can occur as stress concentrators act within the microstructure. To rule local plasticity out entirely, transmission electron microscopy (TEM) would need to be performed on the cracks, and on the crack tips specifically to determine if any dislocations are present and if there is an increased density of dislocations around the crack tip as predicted in the dislocation activity models. If a lack of dislocations is confirmed in the TEM, then these results would rule out dislocation-based LME models, including the dislocation activity liquid metal embrittlement models proposed by Lynch, Rebinder and Popovich, and Hancock and Ives, as all three are dependent on the liquid metal assisted nucleation and motion of dislocations which should not be present under elastic strain conditions.

This result would also seemingly exclude two of the crack tip brittle fracture models, namely the Rostoker-Rehbinder and the SJWK models as both are dependent on dislocation to initiate the cracking behavior. These results would seem to agree with the work of Heesung Kang et. al. as their work showed no particular pileup of dislocations in the fracture surfaces of steels affected by LME (Kang H., Cho, Lee, & De Cooman, 2016).

The second point this thesis reveals about LME is that different types of AHSS do in fact have significantly different LME responses even when they share the same galvanization process. Both the ductility trough and the small strain experiments support this thought. From the ductility trough tests, Figures 10, 13, and 14 show that EG TBF1180 exhibits LME behavior over a wider temperature range than either of the CP1200 samples. This idea is supported by work done by Briant as he was able to show that TBF1180 had a greater drop in fracture energy as a result of LME than CP1200 at temperatures less than 700 °C (Briant, 2018). The difference between steel generations can also be seen in the small strain tests. This difference can partially be seen in Figures 21, 23, and 25 where a comparison of the third generation EG TBF1180 and the first generation EG CP1200 samples shows the TBF1180 samples to generally produce a greater number of cracks. Additionally, these cracks tend to be longer than those found in the electro-galvanized CP1200 samples. Where this is especially apparent, however, is in Figures 22, 24, and 26. In these examinations of the samples tested at 600 °C, at all three strain values the TBF1180 samples have observable cracks while the CP1200 samples do not. The presence of these cracks at 600 °C is contrary to the idea presented by Kang et. al. that the peritectic reaction of iron, zinc, and manganese is necessary for liquid metal embrittlement to occur, as this peritectic is at 782 °C (Kang H., Cho, Lee, & De Cooman, 2016).

The preferential LME of TBF 1180 even at lower temperatures does, however, agree with the idea presented in Briant's thesis that for LME to occur deformation must take place at a temperature at which both the austenite phase and liquid zinc are present (Briant, 2018). This idea is based on the prevalence of LME in steels with austenitic structures such as TWIP steels. (Beal, Kleber, Fabregue, & Bouzekri, 2012). This point is further supported by the analysis of interstitial-free steel performed by Kang et. al. This work showed that for fully-ferritic steels with intentionally low content of austenite promoters (<0.01wt% carbon, manganese, or aluminum) no LME occurred at any temperature. This is likely because for relatively pure iron the austenite transition would not occur until 912 °C which is above the vaporization point of zinc at 907 °C. Because the zinc is vaporized before the austenite transition temperature is reached it would be impossible for both austenite and liquid zinc to be present for interstitial free steel and, based on this hypothesis, LME could not occur. Given these requirements it is sensible that at 800 °C both the EG TBF1180 and the EG CP1200 would exhibit LME, as austenite would first appear in steel at the eutectoid temperature at 727 °C, and the melting temperature of zinc is 420 °C. This temperature produced austenite could couple with any retained austenite in the microstructure to lead to LME occurring in these steels at 800 °C. At 600 °C, however, this effect would have to rely on retained austenite in order to produce an LME effect. This would match neatly with the results, as the TBF1180, which has a microstructure of a mixture of retained austenite and bainite (Lee & Han, 2015), cracked in the presence of deformation and liquid zinc, while the CP1200, which has no retained austenite (Kuziak, Kawalla, & Waengler, 2008), did not.

The third major point addressed by this thesis is that the method of galvanization can have a substantial effect on the LME behavior of a steel. Comparisons made between (c) and (d)

of Figure 21, (b) and (c) of Figure 23, and (b) and (c) of Figure 25 show that for all strain values hot-dip galvanized CP1200 shows a greater effect of LME than electro-galvanized CP1200. In all cases examined, the GI CP1200 displays not only a greater number of LME cracks nucleated, but that the individual cracks are longer and more developed than their counterparts in the EG CP1200 samples. Results in the literature would support this idea, as Tolf et. al. found that in the resistance spot welding of samples of electro-galvanized and hot-dip galvanized DP600 steel the hot-dipped samples were more likely to form surface LME cracks. Tolf et. al. suggest that this cracking occurs when aluminum in the hot-dip coating forms aluminum oxide increasing the electrical resistance and temperature of the weld, encouraging LME (Tolf et. al., 2013). This mechanism could not, however, be the case for the experiments conducted in this thesis as the hot-dipping process is carried out in pure zinc. Instead, the increase in LME sensitivity in the GI CP1200 may be as a result of the creation of certain iron-zinc intermetallics formed during the hot-dip galvanization process. Figure 28 shows a schematic view of the complex, layered intermetallic structure of hot-dip galvanized steel.



Figure 28. The simplified structure of hot-dip galvanized steel adapted from (Mita, Ikeda, & Maeda, 2013)

Based on this representation, during hot dip galvanization a layer of the Γ intermetallic is created at the final interface between zinc and steel. This is important as both H. Kang and J. Kang propose this intermetallic as an important step in the creation of LME conditions. In both studies it is a development of this Γ phase into a zinc rich ferrite structure that precedes LME. J. Kang specifically has LME cracks propagating along micrograins of this zinc rich ferrite that form at the grain boundaries of the steel that form at higher temperatures.

This proposed process is shown in Figure 29. In the testing, samples of galvanized 22MnB5 steel were heated to the temperatures shown below and allowed to anneal for 5 minutes before being pulled at temperature and then cooled quickly to room temperature. By annealing the samples to these target temperatures, tensioning the samples, and examining the samples afterwards the study was able to assess the evolution of the steel-zinc interface and what

microstructures lead to LME cracking. As the temperature is increased initially to 500 °C, zinc and iron atoms diffuse across the interface transforming the majority of the η zinc into the δ intermetallic. Meanwhile, at the interface itself, zinc atoms preferentially diffuse to the grain boundaries of the steel depleting the δ in that area turning it into the Γ intermetallic while enriching the steel grain boundaries with zinc. At 600 °C the Γ intermetallic has grown by diffusing enough zinc into the steel grain boundaries that grains of zinc-rich ferrite begin to form at these grain boundaries. Cracks begin to propagate into the steel along the grain boundaries of the zinc-rich ferrite. At 700 °C the Γ intermetallic has overtaken the coating layer. More grains of zinc-rich ferrite form at the steel grain boundaries and the existing grains grow. Additionally, zinc-rich ferrite nucleates in the Γ . Cracks from the brittle coating propagate readily along the grain boundaries of the zinc-rich ferrite into the steel. At 800 °C the zinc-rich ferrite grains have grown and nearly overtaken the Γ intermetallic. Cracks initiate in the coating layer and follow the ferrite into the surface. At 900 °C the ferrite phase has completely engulfed the coating and no cracks are able to form in the comparatively ductile ferrite (Kang J., Kim, Kim, & Kim, 2019).

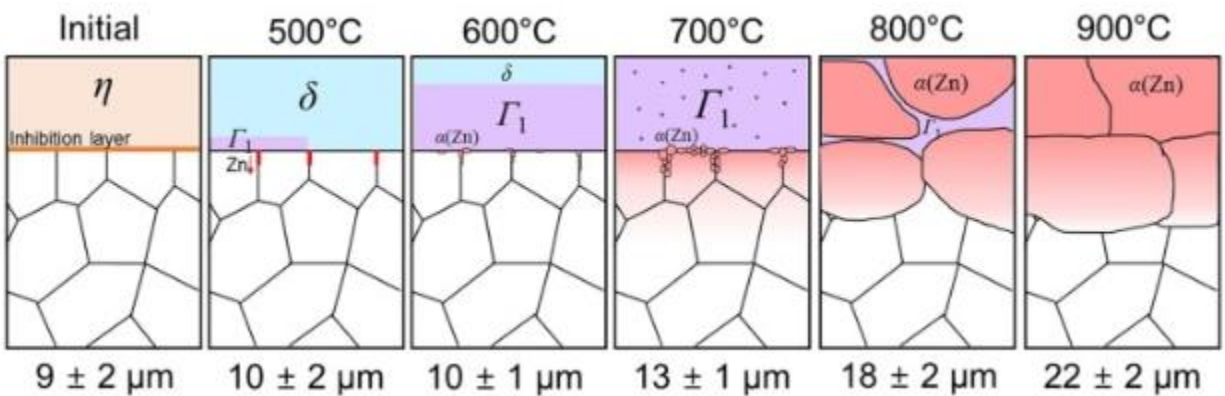


Figure 29. The progression of the zinc-steel interface at increasing temperature (Kang J., Kim, Kim, & Kim, 2019).

The formation of a stable layer the Γ phase during the hot dipping implies that zinc enrichment of the steel grain boundaries may have already occurred in GI CP1200. EG CP1200 starts with a pure zinc coating and must go through a series of reactions to nucleate Γ phase necessary to enrich the steel grain boundaries and nucleate the small grains of zinc-rich ferrite necessary for coating cracks to penetrate the substrate. This head start on the embrittling process could explain why, when compared to EG CP1200, GI CP1200 nucleates a greater number of larger cracks under the same testing conditions. It should also be noted that the 22MnB5 is fully austenitic, and as such cracking can occur at lower temperatures than those seen in either CP 1200 as they contain no retained austenite. The effect of galvanization method on other steels must be examined to confirm this conclusion.

At first glance, the results of the small strain experiments seem to run counter to the ductility trough experiments for the effect of galvanization method, however, as a look at Figures 13 and 14 will show, the ductility trough experiments EG CP1200 demonstrates a greater loss of ductility than GI CP1200 at 800 °C. This is in direct contrast to the results seen in Figures 21, 23, and 25 where the for all small strain test values at 800 °C the GI CP1200 samples contain a greater number of cracks that are larger than those seen in the EG CP1200 samples. One possible explanation for this is that the GI CP1200 is forming so many cracks that the stress is more evenly distributed along the gage section than in EG CP1200 where the stress would be concentrated among fewer cracks. This could increase the compliance for the GI CP1200 sample.

Another explanation for this disparity is the difference in sample preparation method. For the ductility trough experiments an industrial round robin method which removes the zinc from one entire side of the tensile sample, whereas sample preparation for the small strain tests

removes a minimal amount of zinc by sanding away only a small area to attach the thermocouples. The effect of this difference in zinc removal is tested by running the same ductility trough tests on the same GI CP1200 samples, while changing the sample preparation method to that used for the small strain experiments. Figure 30 shows the stress versus strain curves for a bare sample, a round robin sample, and a sample prepared by Beal's method of GI CP1200 tested at 800 °C. As can be seen the Beal method of sample preparation shows a significant loss of ductility when compared to the round robin method. This result holds true across a spectrum of temperatures as well. Figure 31 shows the ductility trough results of these tests compared to those of the previous ductility trough results for GI CP1200. In this graph, the Beal method shows a greater LME effect overall. A possible explanation for these observed differences can be seen in SEM image in Figure 16 (a). In this it can be observed that the fracture surface of a sample of GI CP1200 prepared using the round robin method demonstrates both brittle and ductile behavior. This occurs as the brittle fracture front proceeds from the one side of the sample with a zinc coating while the zinc-free side necks and undergoes a more ductile mode of failure. This difference can also be seen in the EG TBF1180 sample shown in Figure 11, as the magnified image in 11 (b) shows where the brittle, intergranular fracture surface meets the ductile fracture surface indicated by the presence of micro-voids. This joint ductile-brittle failure from the lack of remaining zinc in the round robin method could explain the discrepancy in the effect of galvanization method between the small strain and ductility trough tests.

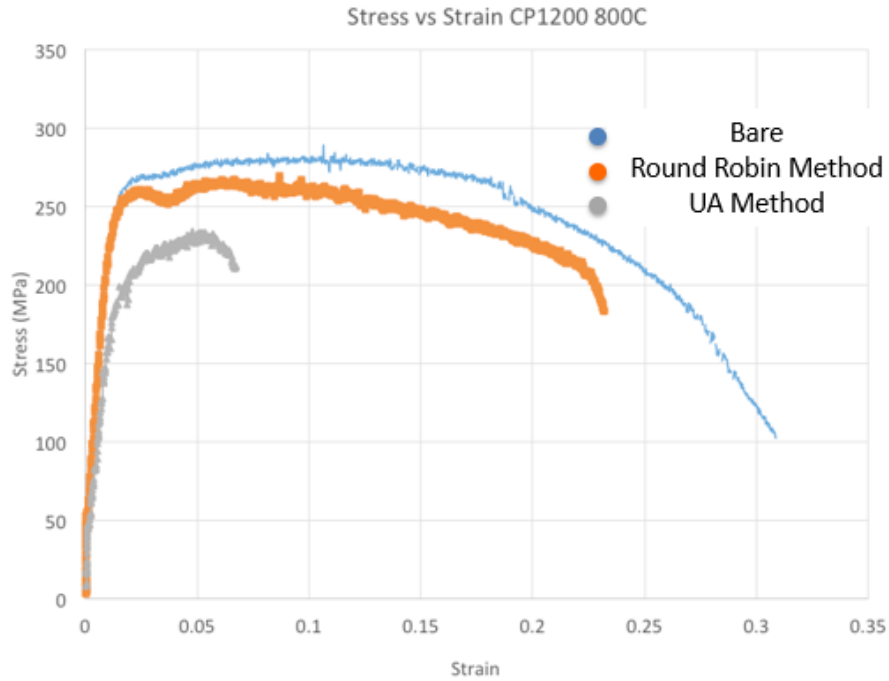


Figure 30. Stress versus strain of failure testing of GI CP1200 with different sample preparation methods at 800 °C

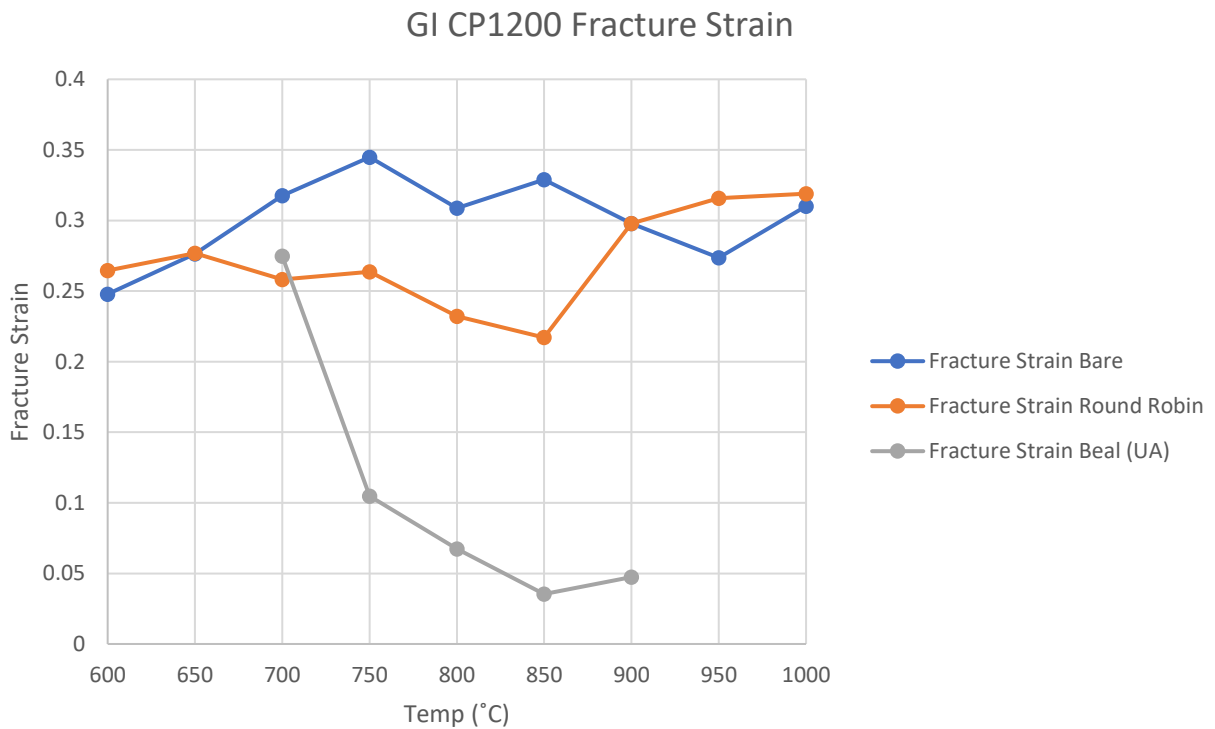


Figure 31. Temperature effect on ductility as measured by fracture strain for GI CP1200 for different sample preparation methods

One final point that must be discussed are the challenges associated with conducting small strain experiments on the Gleeble thermomechanical tester. The Gleeble is a hydraulic tensile testing system as opposed to a screw driven system and therefore must rely on internal feedback loops and hydraulic actuators to do stroke-controlled experiments. As the yield point of each steel is unknown as a function of temperature, the experiments must be performed in strain or stroke control. The requirement for feedback controlled testing combined with friction in the couplings of the load train can lead to ringing in the stroke signal and a certain amount of inaccuracy in the system. This effect balances out over the larger scale tests typically performed on Gleeble machines, and thus the effect is much more noticeable over short stroke tests such as those performed for this thesis. Additionally, there is compliance in the system that must be accommodated before accurate testing can begin. The solution chosen to counter these issues was to record displacements and calculate strains using an extensometer on the sample itself, as this ensures that only displacement experienced by the area of interest is taken into account when recording data. Even with this, special care must be taken in creating the small strain experiments to ensure that desired strain values are reached and data accurate to the materials in question is recorded. The accuracy of the small strain experiments was tested in this thesis by running a room temperature small strain test, checking the linearity of the elastic region, and comparing the measured Young's modulus to known literature values. The results of this test are shown in Figure 32. The R-squared value is very near one, so the test shows the desired linearity in the elastic region. The calculated Young's modulus of 233GPa is higher than the assumed value of 215GPa for a TRIP steel of this strength, yielding a 7.7% error (Fei & Hodgson, 2006). However, given the difficult nature of these small strain tests this error is acceptable.

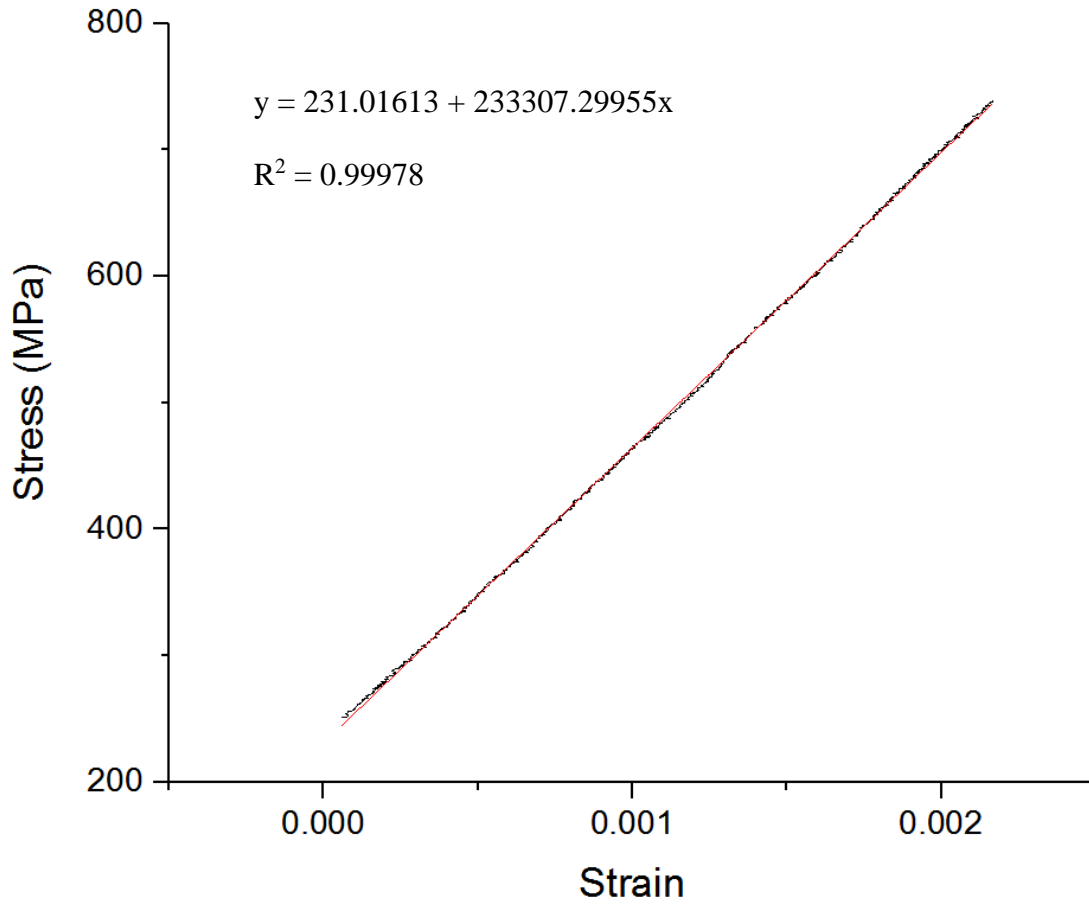


Figure 32. Elastic region of room temperature test of TRIP700 steel with linear fit (red) and a 1kN preload

CONCLUSION

This thesis explores the sensitivity of advanced high strength steels (AHSS) to liquid metal embrittlement (LME) during ductility trough testing and during macro-plastic and macro-elastic small total strain testing. These methods are used to examine the LME response of different AHSS with the same galvanic coating. Additionally, the necessity of macro-plasticity to trigger LME is examined. Finally, the effect of galvanization method on LME sensitivity is examined by comparing samples of the same AHSS galvanized using the hot-dip process and the electro-galvanization process subjected to the same strain tests. This thesis makes the following determinations:

- **LME can occur over a range of temperatures and its severity is temperature and steel dependent.** Depending on the AHSS tested, LME was seen at temperatures as low as 600 °C and up to temperatures exceeding the vaporization point of zinc. Maximum ductility loss occurs between 800 °C and 850 °C. TBF1180 showed LME over a wider temperature range than CP1200 which had an LME response focused at 800 °C.
- **First and third generation AHSS with the same galvanic coating have different LME responses to small strain tests.** EG TBF1180 shows a significantly greater LME response than EG CP1200 both in fracture strain testing and small strain testing. This is likely as a result of the retained austenite in TBF1180 and an assumed requirement of austenite, deformation, and liquid zinc for LME to occur.

- **Macro-plastic strain does not appear to be required for LME to occur.** For all steels tested: EG TBF1180, EG CP1200, and GI CP1200 liquid metal embrittlement cracks occurred at 800 °C even during strain tests where only macro-elastic strain values were measured. No cracking was observed for the CP 1200 steel tested at 600C, while cracking was observed for EG TBF 1180.
- **Galvanization method may have a significant effect on LME sensitivity in an AHSS.** In comparing EG CP1200 and GI CP1200 it can be seen that the GI CP1200 shows a greater LME effect during small strain tests and a greater range of temperature sensitivity during ductility trough tests. This is likely a result of the formation of the Γ ($\text{Fe}_3\text{Zn}_{10}$) intermetallic during the galvanization process, as it has been found that the transformation of this intermetallic to zinc-rich ferrite is a key step in LME. It should be noted that the ductility trough tests did not show as great of a difference between the two galvanization methods.

REFERENCES

- American Galvanizers Association. (2011). Zinc Coatings: A Comparative Analysis of Process and Performance Characteristics.
- Bachmaier, A., Hausmann, K., Krizan, D., & Pichler, A. (2013). Development of TBF Steels with 980 MPa Tensile Strength for Automotive Applications: Microstructure and Mechanical Properties. Linz, Austria: ResearchGate.
- Beal, C., Kleber, X., Fabregue, D., & Bouzekri, M. (2012). Embrittlement of zinc coated high manganese TWIP steel. *Materials Science and Engineering A*.
- Bhattacharya, D. (2018) Liquid metal embrittlement during resistance spot welding of Zn-coated high-strength steels, *Materials Science and Technology*, 34(15), 1809-1829.
- Bouaziz, O., Allain, S., Scott, C. P., Cugy, P., & Barbier, D. (2011). High manganese austenitic twinning induced plasticity steels: A review of the microstructure properties relationships. *Current Opinion in Solid State & Materials Science*, 15(4), 141-168.
- Briant, N. (2018). Investigation of Liquid Metal Embrittlement in Advanced High Strength Steels. Master's Thesis. University of Alabama.
- Cai, X. H., Liu, C. B., & Liu, Z. Y. (2014). Process design and prediction of mechanical properties of dual phase steels with prepositional ultra fast cooling. *Materials & Design*, 53, 998-1004.
- Cambridge University Engineering Department. (2003). Materials Data Book.
- Chen, L., Zhao, Y., & Qin, X. (2013). Some Aspects of High Manganese Twinning-Induced Plasticity (TWIP) Steel, A Review. *Metallurgica Sinica*, 26(1), 1-15.
- De Cooman, B. (2004). Structure-Properties Relationships in TRIP Steels containing carbide free Bainite. *Solid State & Materials Science*, 8(3-4), 285-303.
- De Cooman, B., Estrin, Y., & Kim, S. (2018). Twinning-induced plasticity (TWIP) steels. *Acta Materialia*, 142, 283-362.
- Edmonds, D., He, K., Rizzo, F., De Cooman, B., Matlock, D., & Speer, J. (2006). Quenching and partitioning martensite - A novel steel heat treatment. *Materials Science and Engineering: A*, 438, 24-34.

- Fei, D., Hodgson, P. (2006). Experimental and Numerical Studies of Springback in Air V-Bending Process for Cold Rolled TRIP Steels. *Nuclear Engineering and Design*, 236, 1847-51.
- Glickmann, E. (2011). Dissolution Condensation Mechanism of Stress Corrosion Cracking in Liquid Metals: Driving Force and Crack Kinetics. *Metallurgical and Materials Transactions A*, 42(2), 250–66.
- Gordon, P., An H. (1982). The Mechanisms of Crack Initiation and Crack Propagation in Metal-induced Embrittlement of Metals. *Metallurgical and Materials Transactions A*, 13A, 457–72.
- Grade 22 Low Alloy Steel Handbook: 2-1/4Cr-1Mo, 10CrMo9 10, 622, STPA24. (2005). EPRI, Palo Alto, CA: 2005. 1012840
- Hancock, P., Ives, M. (1971). The Role of Plastic Deformation in Liquid Metal Embrittlement. *Canadian Metallurgical Quarterly*, 10(3), 207–11.
- Hausmann, K. (2014). TRIP-assisted Thin Sheet Steel with a Bainitic and/or Martensitic Matrix: Effects of Alloying Elements and Heat Treatment on Phase Transformations, Microstructure, and Mechanical Properties. TECHNISHCE UNIVERSITÄT MÜNCHEN.
- Joseph, B., Picat, M., Barbier, F. (1999) Liquid metal embrittlement: a state-of-the-art appraisal. *Eur Phys J Appl Phys.*, 5(1):19–31.
- Kang, H., Cho, L., Lee, C., & De Cooman, B. (2016). Zn Penetration in Liquid Metal Embrittled TWIP Steel. *Metallurgical and Materials Transactions*, 47(A), 2885-2905.
- Kang, J., Kim, D., Kim, D.H., Kim, S. (2018). Fe-Zn reaction and its influence on microcracks during hot tensile deformation of galvanized 22MnB5 steel. *Surface and Coatings Technology*, 357, 1069-1075.
- Kim, Y., Kim, I., Kim, J., Chung, Y., & Choi, D. (2014). Evaluation of Surface Crack in Resistance Spot Welds of Zn-Coated Steel. *Materials Transactions*, 55(1), 171-175.
- Klinger, L., Rabkin, E. Theory of Kirkendall Effect During Grain Boundary Interdiffusion. *Acta Materialia*, 59, 1389–99.
- Kuziak, R., Kawalla, R., & Waengler, S. (2008). Advanced high strength steels for automotive industry: a review. *Archives of Civil and Mechanical Engineering*, 8(2), 103-117.
- Lee, Y.-K., & Han, J. (2015). Current opinion in medium manganese steel. *Institute of Materials, Minerals and Mining*, 31.

- Lynch, S. (1988). Environmentally assisted cracking: Overview of evidence for an adsorption-induced localised-slip process. *Acta Materialia*, 36(10), 2639–61.
- Marder, A. (2000). The Metallurgy of Zinc-Coated Steel. *Progress in Materials Science*, 45, 191-271.
- Mita, K., Ikeda, T. and Maeda, M. (2013). Fundamental Study of Fe-Zn Intermetallic Compounds for Zinc Evaporation from Galvanized Steel Sheet. In *Recycling of Metals and Engineered Materials* (eds D. L. Stewart, J. C. Daley and R. L. Stephens).
- Motavalli, J. (2012). For lightweight cars, a materials race, *New York Times*, 10
- Outinen, J. & Mäkeläinen, P. (2002). Mechanical Properties of Structural Steel at Elevated Temperatures and After Cooling Down. *Second International Workshop- Structures in Fire*. 273-290.
- Popovich, V. (1979). Mechanisms of Liquid-Metal Embrittlement. *Fiziko-Khimicheskaya Mekhanika Materialov*, 15 (5), 11–20.
- Rostoker, W., McCaughey, J., Markus, H. (1960) Embrittlement by Liquid Metals. Reinhold Publishing Corporation, New York.
- Silva, E., Fernandes, L., Silva, J., Ribeiro, R., Pereira, M., et. al. A Comparison between an Advanced High-Strength Steel and a High-Strength Steel Due to the Spring back Effect. *IOSR Journal of Mechanical and Civil Engineering*, 13(05), 21-27.
- Tolf, E., Hedegard, J., Melander, A. (2013). Surface Breaking Cracks in Resistance Spot Welds of Dual Phase Steels with ElectroGalvanized and Hot Dip Zinc Coating. *Science and Technology of Joining and Welding*, 18(1).
- Wang, L., & Speer, J. (2013). Quenching and Partitioning Steel Heat Treatment. *Metallography, Microstructure, and Analysis*, 2(4), 268-281.
- Westwood, A., Kamdar, M. (1963). Concerning Liquid Metal Embrittlement, Particularly of Zinc Monocrystals by Mercury. *Philosophical Magazine*, 8, 787–804.
- Zaefferer, S., Ohlert, J., & Bleck, W. (2004). A study of microstructure, transformation mechanisms and correlation between microstructure and mechanical properties of a low alloyed TRIP steel. *Acta Materialia*, 52(9), 2765-2778.